Design, Modelling, and Fabrication of a Low Frequency Piezoelectromagnetic Energy Harvester

by

Egon Fernandes

A thesis

presented to the University of Waterloo

in fulfilment of the

thesis requirement for the degree of

Master of Applied Science

in

Mechanical and Mechatronics Engineering

Waterloo, Ontario, Canada, 2017

Abstract

The growing demand for electricity has put enormous pressure on the current power grid infrastructure and has caused several major blackouts over the past few decades. As a result, there has been a shift towards a modernized “Smart Grid” which uses sensors and wireless communications technology to detect and quickly react to local changes in power usage. Recent advancements in low-power electronics have created opportunities for wireless sensor nodes which typically use batteries as their power supply and only have a lifespan of a few years. The cost to replace the vast amount of batteries can be immense. This paper details a power solution for Smart Grid applications to replace batteries by harvesting energy from current-carrying wires.

A MEMS piezoelectromagnetic energy harvester has been fabricated through screen-printing of PZT on a stainless steel substrate with a centrally-supported meandering geometry. The energy harvesting device was modelled using COMSOL and validated against experimental results. The design goals of a suitable footprint for microelectronic applications and a resonant frequency of 60 Hz were also achieved. The proposed geometry reduced the presence of torsion in the fundamental mode and increased the efficiency of the harvester. The harvester was able to produce 9 μW from a wire carrying 7 Amps at a distance of approximately 6.5 mm. This work resulted in a greater normalized power density than other MEMS based piezoelectromagnetic devices and shows great potential relative to larger devices using bulk piezoelectrics.

Acknowledgements

First of all, I would like to thank Dr. Armaghan Salehian for selecting me and providing me with the opportunity to work on such a challenging and multidisciplinary topic under her supervision. I would also like to thank the other PI's of the funding that supported this research and who also provided me with guidance: Dr. Lan Wei, Dr. David Nairn, and Dr. Hélène Debeda.

I would like to thank all of the members of my research team that not only provided me with research related help but also with emotional support. Thanks to Blake Martin for reviewing my papers and showing me what true patience is. I would like to thank Xiaodong Zhang for his help with the electromagnetic modelling in COMSOL, and Claude Lucat, Sofia Benouakta, Simon Grall, and Isabelle Favre for their help in the fabrication process.

Last but not least, I want to thank my family and Gillian Shi for all of their love and support during my academic endeavors.

Table of Contents

List of Tables ... vii
List of Figures ... viii
1 Introduction ... 1
  1.1 Motivation ... 1
  1.2 Scope of Research ... 2
  1.3 Contribution ... 2
  1.4 Thesis Outline ... 3
2 Literature Review ... 4
  2.1 Vibrations Based Piezoelectric Energy Harvesting ... 4
  2.2 AC Line Piezoelectromagnetic Energy Harvesters ... 4
  2.3 Cantilever beams and lumped-mass electromechanical model ... 7
  2.4 Low frequency vibration harvesting ... 9
    2.4.1 Spiral ... 9
    2.4.2 Zigzag ... 10
    2.4.3 Meandering ... 11
    2.4.4 Elephant ... 13
  2.5 Piezoelectric Fabrication ... 13
3 Energy harvester design, modelling, and simulation ... 15
  3.1 Introduction to Piezoelectromagnetic Conversion ... 15
    3.1.1 Electromagnetic Modelling ... 16
    3.1.2 Piezoelectric modelling ... 17
  3.2 Design considerations ... 18
    3.2.1 Permanent Magnet ... 18
    3.2.2 Piezoelectric material and fabrication ... 18
    3.2.3 Substrate ... 18
    3.2.4 Geometry ... 19
  3.3 Design, modelling, and simulation ... 19
    3.3.1 Design ... 19
    3.3.2 Modelling ... 20
    3.3.3 Simulation ... 23
4 Fabrication, experimental procedure, results, and model validation ... 32
  4.1 Fabrication ... 32
    4.1.1 Screen-Printing Process ... 32

4.1.2 Thick Film PZT Screen-Printing Process 33
4.1.3 Masks and Screens 33
4.1.4 Fabrication Process 35
4.1.5 Issue with fabrication and resolution 40
4.2 Experimental procedure, results, and model validation 43
4.2.1 Experimental Methodology 43
4.2.2 Experimental setup and equipment 43
4.2.3 Base excitation results 44
4.2.4 Electromagnetic testing and results 48
5 Conclusion 60
5.1 Summary 60
5.2 Future work 60
References 62
Appendix 65

List of Tables

Table 1: 301 Stainless Steel Properties 20
Table 2: Neodymium Magnet (NdFeB, N42) Properties 21
Table 3: Screen-printed PZT Parameters 21
Table 4: Compliance matrix for screen-printed PZT 21
Table 5: Coupling matrix for screen-printed PZT 21
Table 6: Relative permittivity matrix for screen-printed PZT 21
Table 7: FEA Meshing Information 22
Table 8: Normalized power density for previous piezoelectromagnetic harvesters and the present work . 57
Table 9: Comparison of quad-folded and centrally-supported meandering designs 66

List of Figures

Figure 1: Schematic of electric power grid ... 2

Figure 2: Schematic and photograph of AC scavenging device ... 5

Figure 3: CAD drawing for the electromechanical AC energy scavenger ... 5

Figure 4: a) Schematic of energy harvester for single wire and b) the Halbach array to concentrate magnetic field on one side ... 6

Figure 5: MEMS AC Energy Harvesters - left: 10x10 mm^2; right: 10x7 mm^2 ... 6

Figure 6: A two-layer bimorph mounted as a cantilever. The top and bottom layers are piezoelectric; bending the beam creates tension in the top layer and compresses the bottom layer ... 7

Figure 7: Model of a kinetic energy harvester structure composed of lumped elements with connected electrical harvesting circuit ... 8

Figure 8: Circuit representation of a piezoelectric generator with a resistive load ... 8

Figure 9: Serpentine structures (a) Basic concept, (b) Double Beam Sandwich, (c) Tethered structure ... 10

Figure 10: The zigzag energy harvesting structure ... 10

Figure 11: Simulated 1-directed strain contour of the proposed meandering energy harvester, showing positive and negative strain locations along the top piezoelectric layer surface ... 11

Figure 12: Simulated open-circuit voltages: a) Single continuous electrode; b) SME; c) SMP ... 12

Figure 13: Schematic showing voltage polarity of strain-matched electrode (SME) and strain-matched polarization (SMP) designs with simplified piezoelectric model. ... 13

Figure 14: Fundamental mode shape and picture of the fabricated device in test step for the Elephant design ... 13

Figure 15: Schematic of the piezoelectromagnetic energy harvester over a conductor ... 16

Figure 16: Dimensioned (mm) schematic of energy harvester substrate ... 19

Figure 17: COMSOL model of Piezoelectromagnetic Energy Harvester ... 20

Figure 18: Fundamental mode shape showing total displacement – a) Top view b) Isometric view ... 23

Figure 19: Fundamental mode shape a) Strain b) Piezoelectric polarization ... 24

Figure 20: Base excitation model ... 25

Figure 21: 2D COMSOL model of infinitely long wire and permanent magnet ... 26

Figure 22: Permanent magnet superimposed on *d(Hy)/y* plot of a single current-carrying wire ... 27

Figure 23: Electromagnetic force for varying magnet length ... 28

Figure 24: Electromagnetic force for varying magnet height ... 29

Figure 25: Electromagnetic force on the magnet vs distance between wire surface and bottom face of magnet ... 30

Figure 26: Electromagnetic force due to varying currents in wire. Distance = 9.3 mm (blue) and 6.8 mm (green) 30
Figure 27: Inputting electromagnetic force to the energy harvester model 31
Figure 28: Screen printing A. Ink. B. Squeegee. C. Image. D. Photo-emulsion. E. Screen. F. Printed image 33
Figure 29: Masks (blank, bottom electrode, PZT, top electrode) 34
Figure 30: PZT Screen 35
Figure 31: DEK Screen-printer 35
Figure 32: Each step of screen-printing process 37
Figure 33: PZT energy harvester fabricated using screen-printing technology 37
Figure 34: Optical profiler used to measure the thickness profile of the harvester 38
Figure 35: a) Cross section of stainless steel substrate with screen printed layers b) Thickness measurement lines across the sample for optical profiling c) Optical profile along A-A d) Optical profile along B-B 39
Figure 36: Peeling of layers in fabricated units 41
Figure 37: Fabricated unit using one firing at very end 42
Figure 38: a) Experimental test setup equipment b) Close up of EH 44
Figure 39: Displacement and voltage FRF of the EH without a tip mass 45
Figure 40: Displacement and voltage FRF of the EH with a tip mass 46
Figure 41: Piezoelectromagnetic energy harvester clamped above a current-conducting wire 48
Figure 42: Experimental test setup of the piezoelectromagnetic energy harvester on a current-conducting wire 49
Figure 43: Tip displacement and voltage FRF showing a resonant frequency at 60.3 Hz 50
Figure 44: Power curves across 10 kΩ to 1 MΩ resistive loads 52
Figure 45: Power output for different load resistances 53
Figure 46: Power output as a function of electric current and distance from wire for the optimal load 54
Figure 47: Voltage frequency responses for increasing wire currents demonstrating non-linear effects 55
Figure 48: Backbone curve of the frequency response. Dots represent the peaks of the experimentally obtained frequency response curves and the solid line represents their best fit quadratic curve 56
Figure 49: Current in the wire (top) and corresponding voltage output of harvester (bottom) 59
Figure 50: Quad-folded cantilever stress plot and assembly for n = 1, 2, 3, 4 65
Figure 51: Centrally supported meandering geometry with 5 beams (left) and 9 beams (right) 66

1 Introduction

This chapter introduces the background and motivation of the research presented in this thesis. It also sets the scope of topics and lists the major contributions of this work to the related fields.

1.1 Motivation

The ever growing demand for electric power has put enormous pressure on the current power grid infrastructure (Figure 1 [1]) and has resulted in several major blackouts over the past few decades. As a result, there has been a shift towards a modernized "Smart Grid" which uses sensors and wireless communications technology to detect and quickly react to local changes in power usage. Various sensors (current, temperature, etc.) are integrated into the smart grid to allow for monitoring of critical components. A vast number of sensors, distributed across the entire grid, are required to adequately monitor the system. Recent advancements in low-power electronics have created opportunities for wireless sensor nodes that combine sensors, power conditioning circuitry, and radios all into one small package and allow for remote sensing. These sensor nodes typically use batteries as their power supply and only have a lifespan of a few years. The cost to replace these batteries can be immense as it not only includes the cost of each battery but also the labor involved to manually change all of the sensor nodes in a network. Moreover, the installation of certain current sensors require a power line to be disconnected and taken out of service which can cause disruptions to the given area. Considering these issues, there is a need to develop a non-invasive, low-cost, and self-powered solution. Energy harvesting is a potential solution to power these wireless sensor nodes.

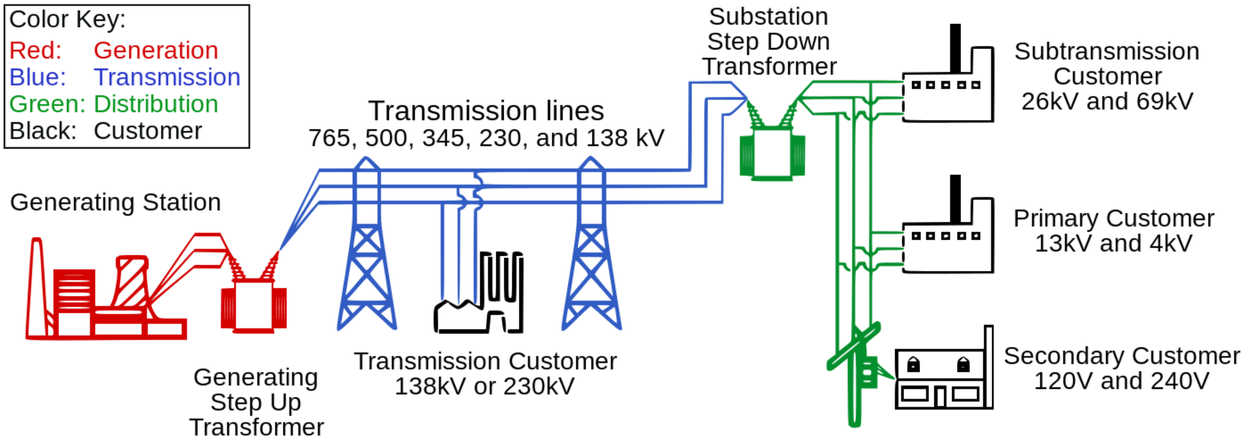

Figure 1: Schematic of electric power grid

1.2 Scope of Research

The purpose of this research is to design a micro-scale energy harvesting unit that can be attached to a power transmission line, couple to the electromagnetic field of the line, and power wireless sensor nodes. The power transmission line belongs to the North American power grid and, thus, operates at a fundamental frequency of 60 Hz with currents ranging from 10 A – 1000 A. However, for this application only current amplitudes of up to 10 A will be used for the proof of concept.

With the energy source clearly defined, the resonance based energy harvester is to be designed and optimized to operate at a frequency of 60 Hz. The harvester is to be cost effective, practical, and micro-scale in size. A finite element model (FEM) is to be developed to predict the mechanical and electrical behavior of the harvester and then to be validated experimentally through prototype fabrication. The optimal load resistance and maximum power output as a function of input current and distance from the wire will also be determined. Voltage regulation and power conditioning circuitry will not be considered in this thesis and are outside the scope of this work.

1.3 Contribution

This research explores a geometry that results in a structure having a low resonant frequency of 60 Hz while maintaining a size in the micro-scale. The thesis provides FEM approach to model and design the energy harvester appropriate for power transmission line harvesting applications and uses micro-electromechanical system (MEMS) fabrication techniques. Optimization efforts are made to maximize the power output of the harvester. This optimization spans areas including geometry and dimensions, choice of substrate and piezoelectric material, choice of magnet and dimensions, and fabrication techniques.

1.4 Thesis Outline

The thesis will be structured in the following manner:

Chapter 2 will be structured into three parts. First will be an overview of common energy harvesting transduction methods. This will provide a foundation for understanding current harvesting advances and key concepts discussed in the second part of the literature review. The next part covers the state of the art geometries used for low frequency mechanical vibrations energy harvesting. With these geometries a type of piezoelectric material is used while maintaining a small footprint. Finally, the different methods of fabrication and their corresponding thicknesses are briefly explained.

Chapter 3 will begin by defining the proposed design based on information gathered from the lit review and scope sections. Fundamentals of operation will be described followed by design optimization. Then the FEA model used to experimentally validate the harvesting unit will be outlined.

Chapter 4 will begin with the experimental methodology and follow with the experimental results gathered. This will be followed by the complete model validations of the design and a discussion of the results.

Chapter 5 will conclude with the results obtained in Chapter 4 and make suggestions for future work in this area.

2 Literature Review

In this chapter, research materials and previous publications are reviewed to provide a thorough understand of existing accomplishments and remaining problems in the related fields. The topics that are reviewed here are vibration and electromagnetic piezoelectric energy harvesting, low frequency harvesting, and piezoelectric fabrication.

2.1 Vibrations Based Piezoelectric Energy Harvesting

Vibration-based harvesting has received increased attention over the past decade due to the reduced power requirements of small electronic components. A few forms of vibration based energy harvesting include electromagnetic, electrostatic, and piezoelectric. Piezoelectric harvesting has the main advantage of large power densities and ease of application [2]. Piezoelectrics also have usable voltage outputs that can directly charge a storage component. Electromagnetic energy harvesting, on the other hand, produce very low voltage outputs and often a multistage post-processing is required. Electrostatic energy harvesting requires an external voltage or charge to be applied to the capacitor element to provide the relative vibratory motion that produces an alternating electrical output. The voltage output of piezoelectric energy harvesting results from its constitutive behavior of the material, which eliminates the needs for an external voltage input. Piezoelectric devices can be fabricated both in macro-scale and micro-scale due to well established thick-film and thin-film fabrication techniques. The poor properties of planar magnets and the limited number of turns using planar coils are practical limitation in enabling micro-scale electromagnetic energy harvesters.

2.2 AC Line Piezoelectromagnetic Energy Harvesters

Vibrations based piezoelectric energy harvesting is a possible solution to power wireless sensor nodes for Smart Grid applications. Extensive research has been done in low-frequency electromagnetic vibration energy harvesting [3]. Previous work with piezoelectric cantilever beams has shown that both current sensing [4] and energy harvesting [5] are possible directly from AC conducting wires using non-invasive technology. The idea applied the technology shown in Figure 2 to single and dual-cord conductors. The work used a piezoelectric bimorph and a high-strength NdFeB magnet. The scavenger’s maximum power output was 208 μW to a 491 kΩ from 9.4 A of current from a space heater cord.

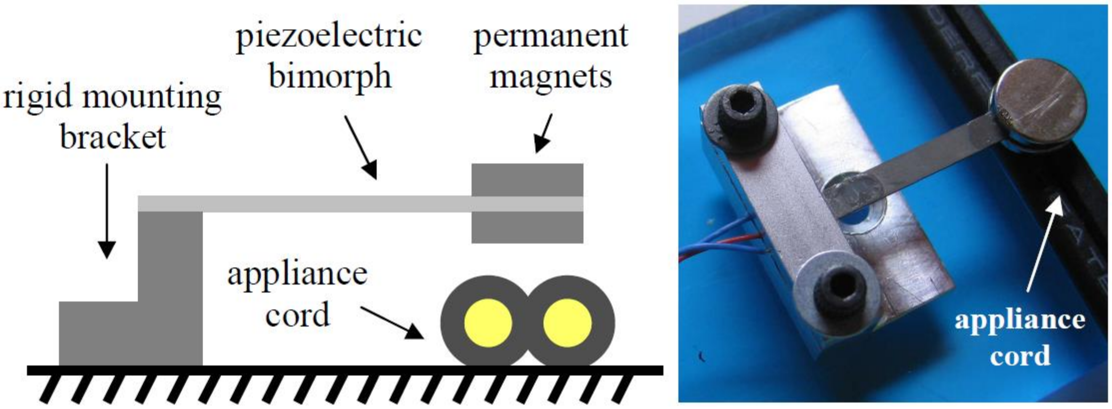

Figure 2: Schematic and photograph of AC scavenging device

This work continued, was improved upon, and compared to coil-based AC scavengers [6]. The work showed that the piezoelectromagnetic approach (Figure 3) is an attractive alternative to AC energy scavenging for applications where the scavenger cannot encircle the current-carrying.

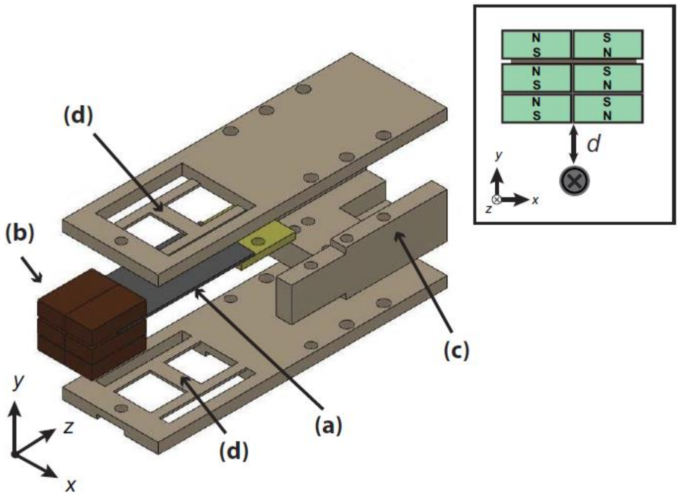

Figure 3: CAD drawing for the electromechanical AC energy scavenger

The concept behind the AC energy harvester was expanded upon by using a “Halbach array” magnet configuration to focus the magnetic field to one side of the overall mass [7]. This way, the electromagnetic force between the magnet array and the current-carrying wire is increased by more than three times.

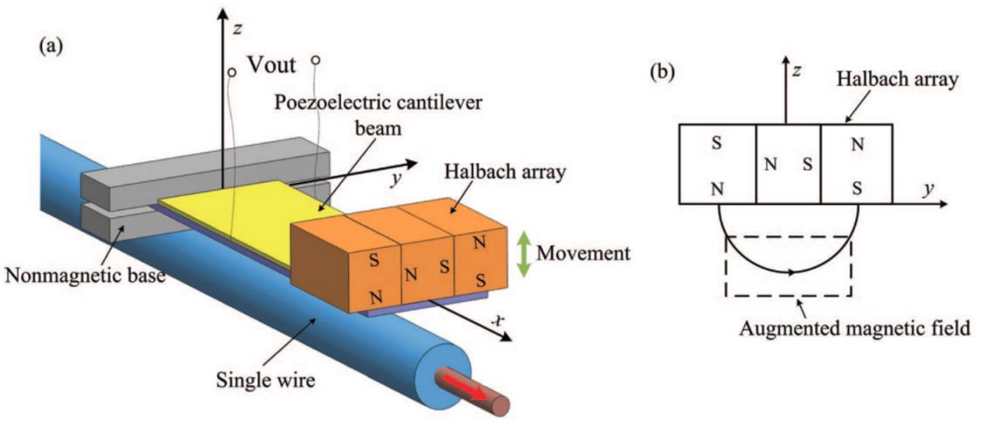

Figure 4: a) Schematic of energy harvester for single wire and b) the Halbach array to concentrate magnetic field on one side

These AC energy harvesting solutions need to scale down to the micro-scale before becoming ubiquitous in the Smart Grid. Micro-electromechanical system (MEMS) solutions allow for mass production which result in lower overall cost per unit. Also, at the MEMS-scale a smaller permanent magnet can be utilized and brought closer to the wire to improve the power density of a harvester.

A MEMS-scale harvester with a footprint of 10x10 mm^2 was modelled and showed the potential to produce 2 μW [8]. The harvester featured a quad-folded cantilever design (Figure 5 left) and a fabrication process was created using Aluminum Nitride (AlN) as the piezoelectric material. More recently, an AlN cantilever (Figure 5 right) with a footprint of 10x7 mm^2 was fabricated and shown to produce 1.5 μW [9].

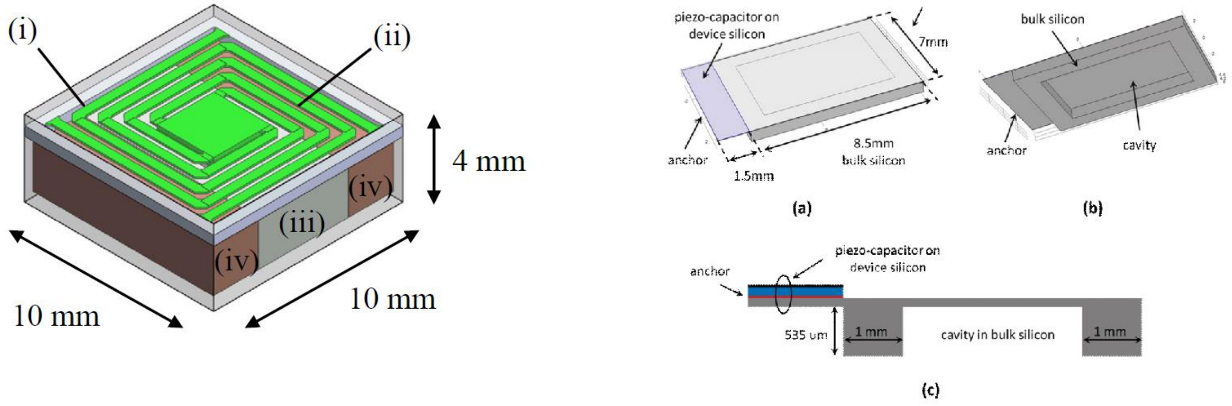

Figure 5: MEMS AC Energy Harvesters - left: 10x10 mm^2; right: 10x7 mm^2

2.3 Cantilever beams and lumped-mass electromechanical model

Most piezoelectric energy harvesters are in the form of cantilever beams and they are one of the most studied configurations for energy conversion. The beams typically consist of one or two piezoceramic layers (unimorph or bimorph) bonded to a flexible substrate. A mass is typically added to the end of the beam to both tune the resonant frequency of the system and also increase the power output. The harvester is located on a vibrating structure and strain is induced in the piezoelectric layer which results in an alternating voltage output across their electrodes. A diagram showing a piezoelectric cantilever beam is shown in Figure 6 [10].

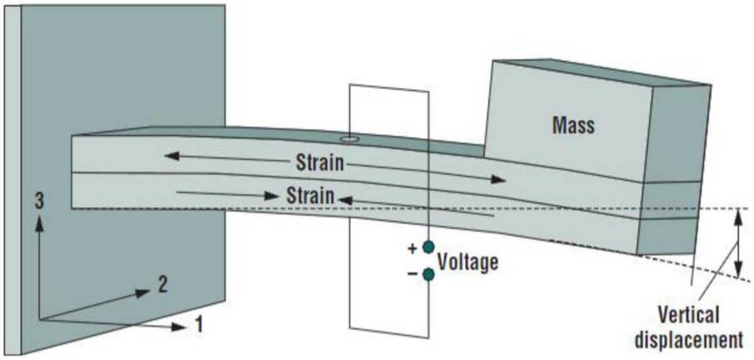

Figure 6: A two-layer bimorph mounted as a cantilever. The top and bottom layers are piezoelectric; bending the beam creates tension in the top layer and compresses the bottom layer

The piezoelectric cantilever system can be modelled using lumped mass parameters coupled with electrical loop equations [11], [12]. An example of a mass-spring-damper representation of the piezoelectric cantilever beam is shown in Figure 7 [13].

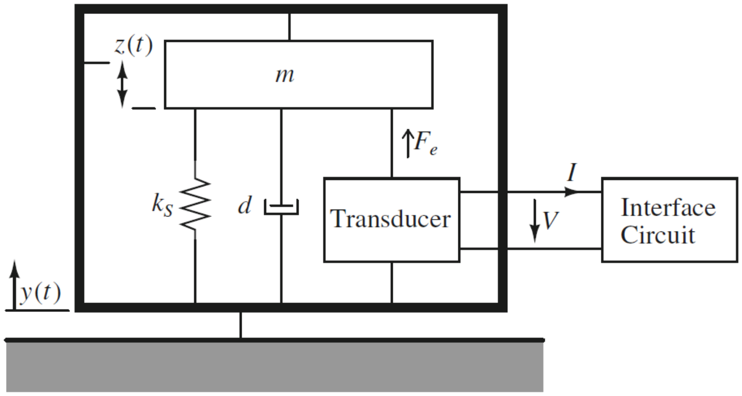

Figure 7: Model of a kinetic energy harvester structure composed of lumped elements with connected electrical harvesting circuit

An electrical analogy can be made and includes an interface circuit [14], as seen in Figure 8. Usually a resistive load is used to measure the power output of the system.

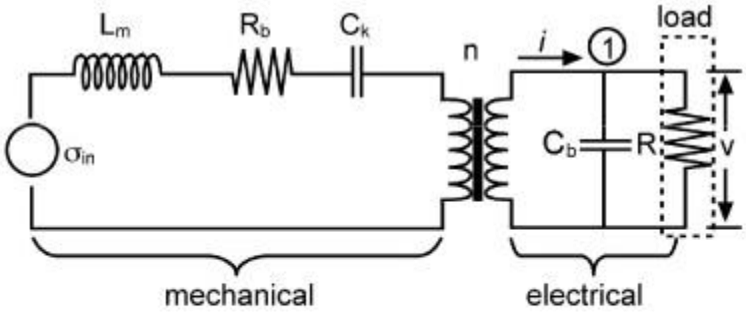

Figure 8: Circuit representation of a piezoelectric generator with a resistive load

A mass is usually attached to the tip of the cantilever to tune the resonant frequency of the system and increase the power output.

The natural frequency of a cantilever beam with a tip mass can be calculated with the following formula [2]:

$$\omega_n = \sqrt{k_{eq}/m_{eq}} = \sqrt{\frac{3YI/L^3}{\left(\frac{33}{140}\right) mL + M_t}} \tag{1}$$

where k_{eq} and m_{eq} are the equivalent stiffness and mass, YI is the flexural rigidity of the beam, L is the length of the beam, m is the mass per unit length, and M_t is the tip mass [15]. For energy harvesting it is critical that the natural frequency of the harvester matches that of the excitation frequency as this results in the maximum power output. In fact, the resulting power output diminishes by orders of magnitude as the frequency shifts by even a few hertz. This is one of the issues with MEMS-scale harvesting as the natural frequency scales up as the size scales down.

2.4 Low frequency vibration harvesting

Regarding tuning, the main ways the resonant frequency can be reduced is by either decreasing the spring constant or increasing the mass. A few typical ways of decreasing the resonant frequency are:

1) Increasing the beam length

2) Decreasing the thickness

3) Decreasing the width

4) Increasing the tip mass

Certain applications pose tight size constrains on these design parameters which limit the flexibility for tuning. MEMS applications, for example, may only allow for a harvester with an area of under 1 inch^2. The length constraint would typically result in a resonant frequency much higher than 100 Hz and pose a serious drawback in the development of MEMS scale energy harvesters since ambient mechanical vibrations are usually lower than 100 Hz. The following sections detail methods of reducing the spring constant through the use of specific geometries.

2.4.1 Spiral

A long cantilever can be folded into a serpentine cantilever structure (or spiral), as seen in Figure 9, to overcome the MEMS size constraints and maintain a low frequency [16]. Research has shown that the length of the spiral needs to be at least half a turn to obtain a low frequency, and the vibration of these long spirals is dominantly torsional [17]. Other work has tried to increase the output of the spiral cantilever by using hybrid technologies [18] but the intrinsic issue with the main mode of vibration remains.

Figure 9: Serpentine structures (a) Basic concept, (b) Double Beam Sandwich, (c) Tethered structure

2.4.2 Zigzag

A zigzag geometry (Figure 10) is a 2-dimensional cantilever structure that reduces the natural frequency by increasing the effective length [19]. It can be used in energy harvesting for MEMS devices because it can achieve resonant frequencies in the range of ambient energy signals. The zigzag can deflect out of the main plane and be modeled as a few straight beams, with rectangular cross sections, placed next to each other on the main plane. Each beam is connected to its neighbor beams at its ends. The beams can bend out of the main plane and can twist. Each beam is comprised of a piezoelectric layer bonded to a substrate layer (which is usually metallic). When the beams deflect, strain occurs in the piezoelectric layer, which generates electrical energy.

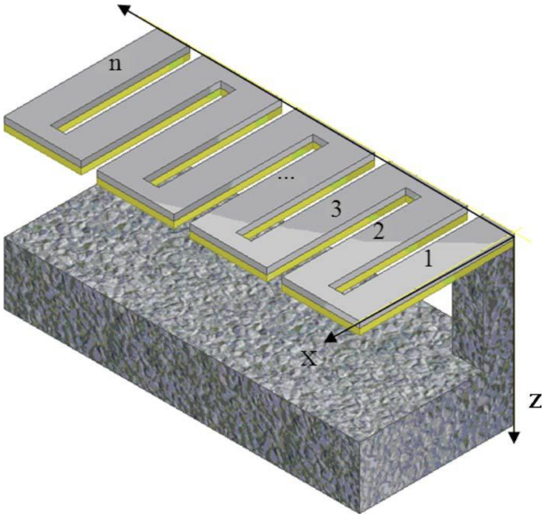

Figure 10: The zigzag energy harvesting structure

The zigzag can outperform 1D cantilever beams in terms of power density and low resonance frequency for a given surface area [20]. The fundamental bending mode shape of the zig-zag includes bending and torsion. As the number of elements increases, the torsion related natural frequencies decrease faster than the bending modes. It was found that after ten beam members the fundamental mode shape becomes dominantly torsional. Since with energy harvesting we are interested in bending vibrations, the zigzag should be limited to less than ten members.

2.4.3 Meandering

The “meandering” geometry (Figure 11) applies symmetry about the free end of a zigzag [21]. The fixed-fixed design experiences reduced torsion at the anchor in comparison to the fixed-free zigzag design. The meandering structure reduces the spring constant when compared to a similar length straight fixed-fixed beam, which results in a lower resonant frequency and lower maximum displacement. Due to the nature of the boundary conditions, the resonant frequency of the meandering geometry is typically higher than similar fixed-free structures. However, the meander structure has been shown to experience 1.3 times lower shear strain at the anchor points and connections between the meander segments than a free-fixed zig-zag structure made of half of the meander.

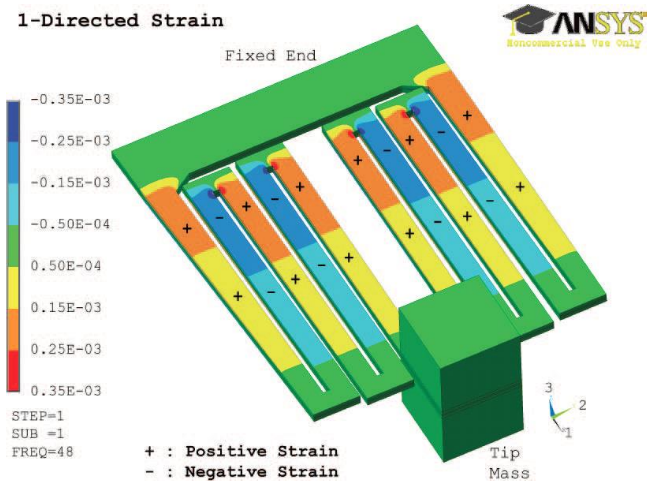

Figure 11: Simulated 1-directed strain contour of the proposed meandering energy harvester, showing positive and negative strain locations along the top piezoelectric layer surface

Strain nodes are found at each beam connection in the meandering geometry and having one continuous electrode would result in a diminished voltage output, as seen in Figure 12a below. A strain-matched electrode and strained-match polarization scheme have been proposed to mitigate the effects of voltage cancellation.

The strain-matched electrode (SME) scheme uses two electrodes: one to cover the beams with all the positive strain and another electrode to cover the beams with like negative strain. The two electrodes are electrically isolated at the strain nodes (beam connections) to avoid the cancellation of positive and negative voltages, as seen below in Figure 12b.

The strain-matched polarization (SMP), Figure 12c, scheme matches the polarization of the piezoelectric material to the strain of the beam. This way the voltage polarity of certain beams is inverted so that all electrodes will have the same voltage polarity. The SMP can use one continuous electrode across the entire piezoelectric material, and does not need complicated wiring between the electrodes like the SME design.

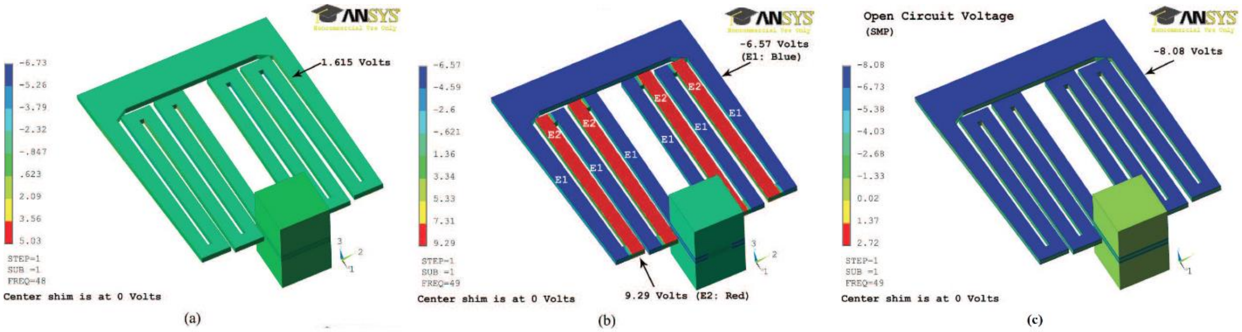

Figure 12: Simulated open-circuit voltages: a) Single continuous electrode; b) SME; c) SMP

Results from this work showed the SMP design achieved slightly higher power output than the SME design because of its lower damping. The higher damping of the SME is potentially due to the soldered wires connected the electrode segments and variations in fabrication. Furthermore, in the SME design, the piezoelectric layers are connected in series, which results in the addition of their voltages. The SMP design, however, has all the piezoelectric layers all connected in parallel, which results in higher current rather than higher voltage like the SME design. The higher voltage of the SME design also results in a higher source impedance which requires a larger load resistance for matching. The schematic showing the voltage polarities of the two designs are shown below in Figure 13.

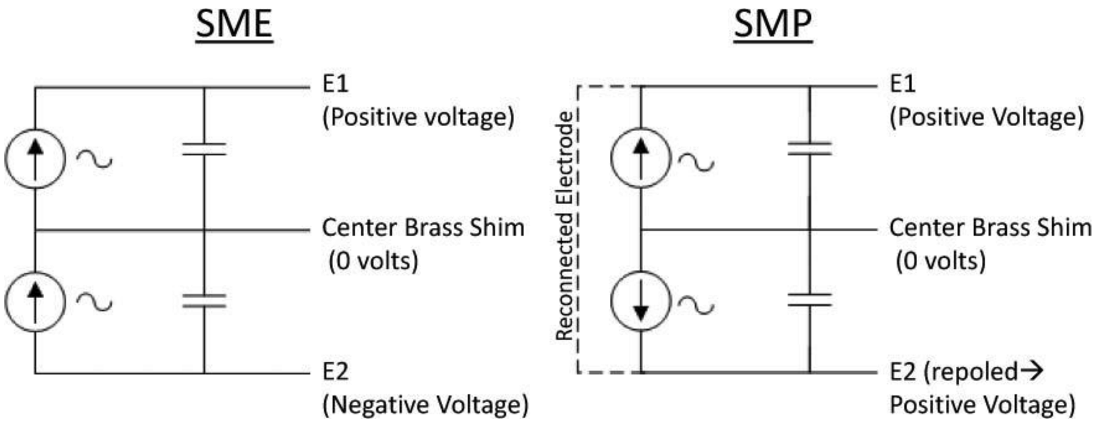

Figure 13: Schematic showing voltage polarity of strain-matched electrode (SME) and strain-matched polarization (SMP) designs with simplified piezoelectric model.

2.4.4 Elephant

The "Elephant" design (Figure 14) proposed by [22] applies symmetry to the zig-zag about its fixed-end, resulting in a fixed-free cantilever like structure. The free-ends are joined to form a closed-circuit symmetric meandering configuration. The purpose of this design is to focus the stress of the system near the clamp and harvest energy only from that area. The design also makes use of symmetry to reduce torsion and allow for more pure bending in the central beam, therefore increasing the harvesting efficiency. The electromechanical coupling coefficient of the Elephant harvester was found to be much larger than that for a zigzag of similar dimensions, which resulted in the Elephant producing more power.

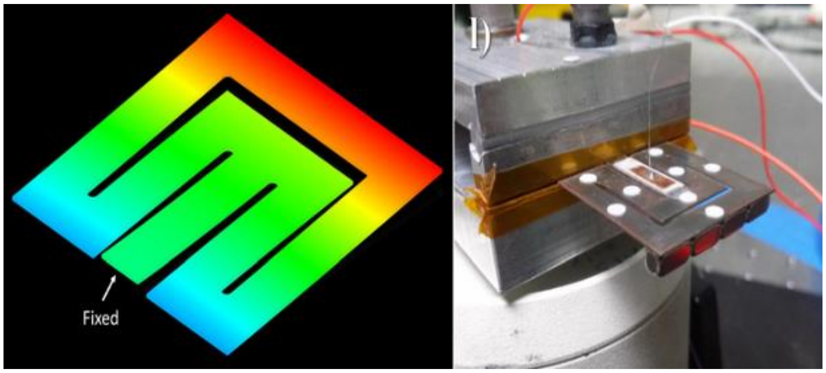

Figure 14: Fundamental mode shape and picture of the fabricated device in test step for the Elephant design

2.5 Piezoelectric Fabrication

For energy harvesting it is critical to use a material with a high electromechanical coupling. For this reason lead zirconate titanate (PZT) is usually selected. Different fabrication methods are capable of yielding different levels of thickness and each has their own limitations. The manufacturing of bulk PZT results in material with the highest electromechanical coupling and is commercially available in thicknesses greater than 100 μm. They are also limited to simple shapes like discs, plates, and rings. Outside of simple shapes, bulk PZT may require expensive micromachining steps for specific applications requiring custom geometries.

Thin film technology allows for piezoelectric layers in the sub-micron range (≤ 1μm). Thin films are not suitable for applications where large forces or deflections are involved. Furthermore, due to their weak electromechanical properties they make poor energy harvesters.

PZT thick-films have been found to make good candidates for MEMS applications due to their higher coupling, and can bridge the 1-100 μm gap between thin film and bulk components [23]. They can be formed by screen-printing through a mask. Free-standing thick-film structures can be mass produced and do not need to be assembled manually, like with ceramics. It is therefore possible to create quite complex structures with a series of relatively simple fabrication steps. They can also be integrated with other thin or thick-film layers and microelectronic components, thereby offering an appealing approach for MEMS-scale energy harvesters. The screen-printing method is a low-cost alternative process to classical silicon manufacturing. The most valuable advantages of screen-printing are the low investment costs for equipment and choice of materials including the substrate and paste.

3 Energy harvester design, modelling, and simulation

Chapter 3 presents the design and modeling of the piezoelectromagnetic energy harvester. Here, the working principle is applied to a centrally-supported meandering design using screen-printed fabrication techniques to lower the resonant frequency to match that of power flow in the North American power grid. Simulations for the eigenfrequency and frequency response analyses are shown as well as the electromagnetic modeling.

3.1 Introduction to Piezoelectromagnetic Conversion

Figure 15 illustrates the design and working principle of the piezoelectromagnetic energy harvester. The harvester is composed of a piezoelectric layer sandwiched between two electrodes on a metallic substrate with a permanent magnet attached to its tip. The harvester is mounted above an AC-carrying wire in a cantilever-like manner where it is fixed at one end. The magnet couples to the alternating magnetic field produced by the wire. A sinusoidal electromagnetic force excites the cantilever and causes the piezoelectric material to experience elastic deformation. Through the piezoelectric effect a voltage is generated across the electrodes. When the harvester is connected to an electrical load, an electric current will flow. The power produced can be calculated as the square of the root mean square (RMS) voltage across the load divided by its resistance. If the frequency of the electromagnetic force matches the resonant frequency of the harvester, the amplitude of the output power will be maximized.

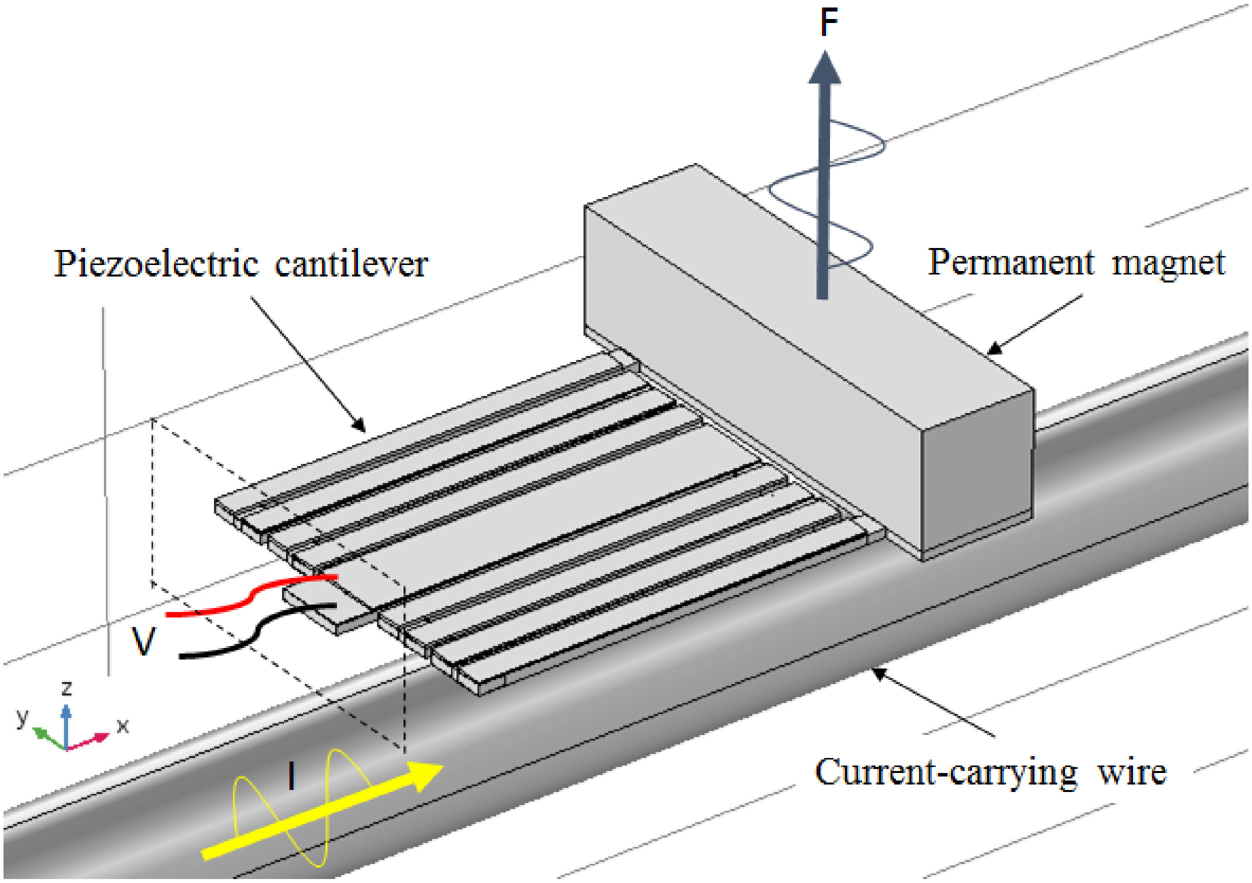

Figure 15: Schematic of the piezoelectromagnetic energy harvester over a conductor

3.1.1 Electromagnetic Modelling

Overhead power lines can be modelled as infinitely-long straight conductors. The derivative of the z-component of the magnetic field along the z direction can be derived as [24],

$$\frac{dH_z}{dz} = \frac{I}{2\pi} \frac{2yz}{(y^2 + z^2)^2}, \tag{2}$$

where I is the current in the conductor, y and z are the distances from the conductor to the points on the magnet in the y-direction and z-direction, respectively. For the coupling to be maximized, the permanent magnets should be placed such that $\frac{dH_z}{dz}$ is maximized. For a single conductor the optimal magnet placement occurs when the poles of the magnet overlap with a 45° line from the center of the conductor and the distance between the two is minimized.

An alternative way to obtain the electromagnetic force experience by the magnets, F_z^M, is to find the reaction force on the conductor, F_z^C. According to Newton's Third Law, these two forces are equal in magnitude and opposite in direction,

$$F_z^M = -F_z^C, \tag{3}$$

According to the Lorentz force law, the magnetic force experienced by the conductor is given by,

$$F_z^C = \oint_V \boldsymbol{J} \times \boldsymbol{B} dV, \tag{4}$$

where **J** is the current density (current divided by the cross-sectional area) and **B** is the magnetic field applied by the permanent magnet. Finally, if just the *z* component of the force is of interest, the magnetic force on the magnet can be derived as,

$$F_z^M = -J_x \oint_V B_y dV = -\frac{I}{A_c} \oint_V B_y \, dV, \tag{5}$$

where B_y is the y-component of the magnetic field produced by the magnet.

3.1.2 Piezoelectric modelling

The magnetic force described above gets applied to the tip of the cantilever along the z-axis. The force generates tensile or compressive strains along the x-axis in the bending elements. With the piezoelectric material being poled in the z-axis, the piezoelectric constitutive equations can be described according to the strain-charge form,

$$S_1 = c_{11}^E T_1 + d_{31} E_3 \tag{6}$$

$$D_3 = d_{13} T_1 + \epsilon_{33}^T E_3 \tag{7}$$

where *S* is strain, *T* is stress, d_{13} is the piezoelectric coefficient in the Strain-Charge form, *D* is the electric displacement, *E* is the electric field, ϵ^T is the permittivity under constant stress, and c^E is the compliance under constant electric field.

The piezoelectric effects can also be described in terms of voltage and force. Rewriting the constitutive equations in the Force-Charge form,

$$F = \Gamma_2 V + Kz, \tag{8}$$

$$Q = C_p V + \Gamma_2 z, \tag{9}$$

where F is the applied tip force, Γ_2 is the coupling coefficient in the Force-Charge form, K is the equivalent spring constant of the cantilever, z is the tip displacement, Q is the accumulated charge, V is the voltage across the electrodes, and C_p is the capacitance of the piezoelectric layer.

3.2 Design considerations

3.2.1 Permanent Magnet

The role of the permanent magnet is two-fold. First, it is used to couple to the electromagnetic field of a current-carrying wire. Maximizing the efficiency of the coupling will result in a higher electromagnetic force and a greater energy harvested.

As the resulting force is directly proportional to the magnetic flux density of the permanent magnet, it is necessary to select a magnet with the highest possible value. NdFeB magnets [25] have been selected for this reason and for their relatively high density.

The magnet also serves as a proof mass that can be used to tune the natural frequency of the system. As this EH uses resonance to maximize the energy harvested from the wire, the mass of the magnet must bring the resonant frequency down to 60 Hz. Theoretically, a larger mass will result in more kinetic energy harvested but the size constraints of the harvester limit the dimensions of the magnet.

3.2.2 Piezoelectric material and fabrication

Since piezoelectric material has been selected for the method of energy transduction, it is necessary to select a piezoelectric material that demonstrates high electromechanical coupling but one that is also suitable for a MEMS fabrication process. PZT is known to have one of the highest coupling factors for a piezoelectric material, and the various available fabrication processes allow it to be manufactured in the micro-range thickness. The screen-printing process allows for thick-films (1-100μm) to be deposited and allow for complicated geometries [26].

3.2.3 Substrate

Since the target natural frequency is relatively low, a substrate material with a low Young's modulus should be selected to ensure minimal additional stiffness is added to the EH. The substrate should also be conductive and suitable for cyclical stress. Finally, the melting point of the substrate material needs to be high enough to withstand the firing process of the fabrication. Thus, for compatibility with the screen-printing fabrication process the substrate will need to have a melting point that is much higher than 900 degrees Celsius.

3.2.4 Geometry

The geometry of the harvester is an extremely important design consideration. Due to the size constraint of the application the geometry must achieve a low natural frequency while maintaining a high power density. As discussed earlier, a cantilever beam's natural frequency rises as the length of the beam decreases. Utilizing a 2-dimensional cantilever beam, such as demonstrated in the zig-zag design, achieves a lower natural frequency by increasing the effective length of the beam. As the number of beams increases in the zigzag design the fundamental mode of vibration switches from bending to torsion. As mechanical vibrations are more efficiently harvested through bending, the geometry must achieve a bending fundamental mode shape and have low torsional contributions.

3.3 Design, modelling, and simulation

3.3.1 Design

The objective of the geometry is to maximize the power density while maintaining a low fundamental frequency in the range of 60 Hz to match the fundamental frequency of the North American power grid. A centrally-supported meandering geometry is used in the current work and is shown in Figure 16 [27].

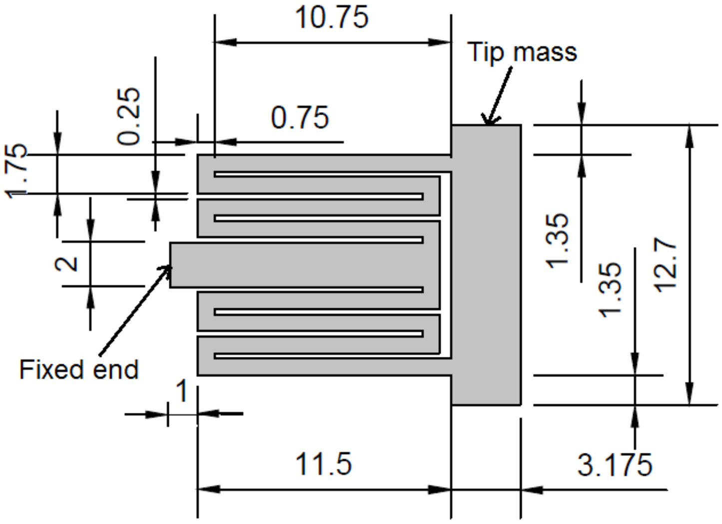

Figure 16: Dimensioned (mm) schematic of energy harvester substrate

The energy harvester occupies an area of 14.675 mm x 12.7 mm or 186 mm^2, excluding the extra space near the clamp that is used for fine-tuning the resonant frequency. A 0.254 mm thick 301 grade stainless steel substrate supports 75 μm thick strips of PZT on each beam. PZT is chosen as the piezoelectric material for its high electromechanical coupling. A fixed-end boundary condition is imposed by clamping one end of the center beam. The remainder of the structure is unrestricted and a magnetic proof mass is attached to the opposite end to tune the natural frequency. A neodymium magnet (Grade N42, B_R = 1.32T) is chosen as the tip mass for its strong magnetic properties and off the shelf availability.

The proposed geometry delivers nearly pure bending to the clamped beam where the majority of the stress is located as shown in [20]. The fixed-free boundary conditions typically result in much lower resonant frequencies than a fixed-fixed system. The geometry also minimizes the area of strain nodes, which results in a greater harvestable area.

3.3.2 Modelling

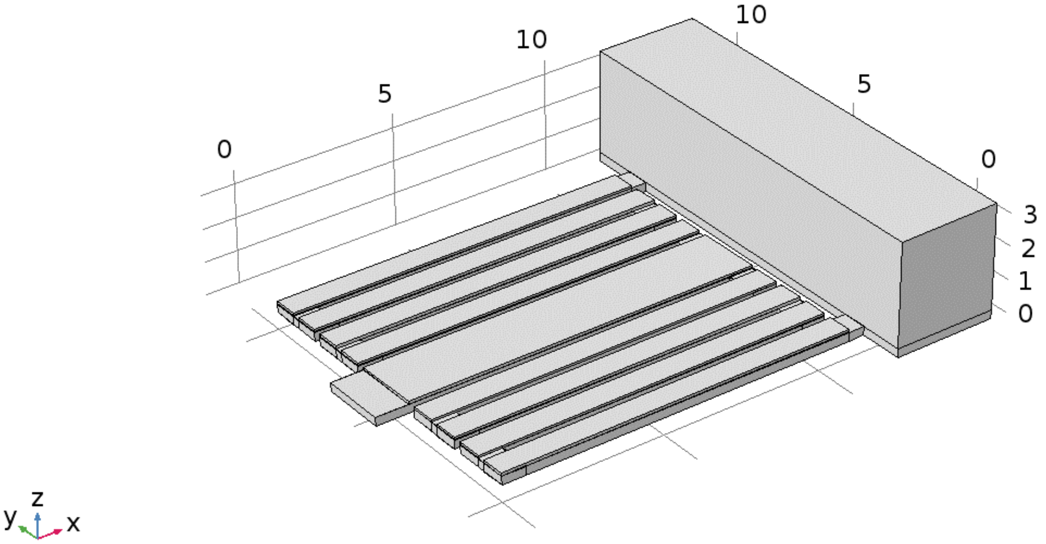

Figure 17: COMSOL model of Piezoelectromagnetic Energy Harvester

The energy harvester (Figure 17) is modelled using the 3D FEA analysis software COMSOL Multiphysics and its associated MEMS module. The structural properties of the stainless steel and the neodymium magnet have been obtained from manufacturers [28], [25] and are presented in Table 1 and Table 2. The screen-printed PZT is an electromechanical material and its properties were determined experimentally [29]. The material properties of the PZT are presented in Table 3-6.

Table 1: 301 Stainless Steel Properties

Young's Modulus	193 GPa
Density	7880 kg/m^3
Poisson's ratio	0.24

Table 2: Neodymium Magnet (NdFeB, N42) Properties

Young’s modulus	160 GPa
Density	7500 kg/m^3
Poisson’s ratio	0.24
Dimensions	3.175 mm x 3.175 mm x 12.7 mm
Weight	0.96 g

Table 3: Screen-printed PZT Parameters

Young’s modulus	43 GPa
Density	5500 kg/m^3
Piezoelectric charge coefficient	-40 pC/N

Table 4: Compliance matrix for screen-printed PZT

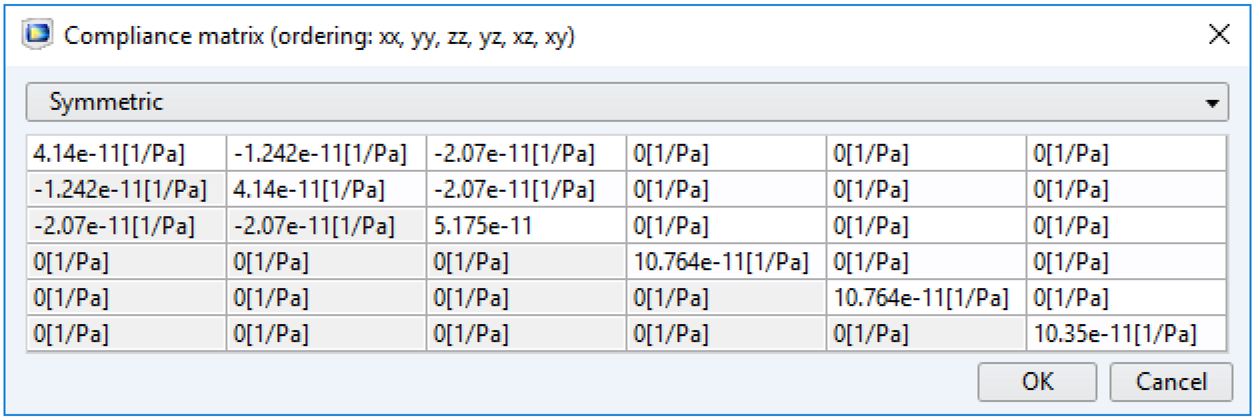

4.14e-11[1/Pa]	-1.242e-11[1/Pa]	-2.07e-11[1/Pa]	0[1/Pa]	0[1/Pa]	0[1/Pa]
-1.242e-11[1/Pa]	4.14e-11[1/Pa]	-2.07e-11[1/Pa]	0[1/Pa]	0[1/Pa]	0[1/Pa]
-2.07e-11[1/Pa]	-2.07e-11[1/Pa]	5.175e-11	0[1/Pa]	0[1/Pa]	0[1/Pa]
0[1/Pa]	0[1/Pa]	0[1/Pa]	10.764e-11[1/Pa]	0[1/Pa]	0[1/Pa]
0[1/Pa]	0[1/Pa]	0[1/Pa]	0[1/Pa]	10.764e-11[1/Pa]	0[1/Pa]
0[1/Pa]	0[1/Pa]	0[1/Pa]	0[1/Pa]	0[1/Pa]	10.35e-11[1/Pa]

Table 5: Coupling matrix for screen-printed PZT

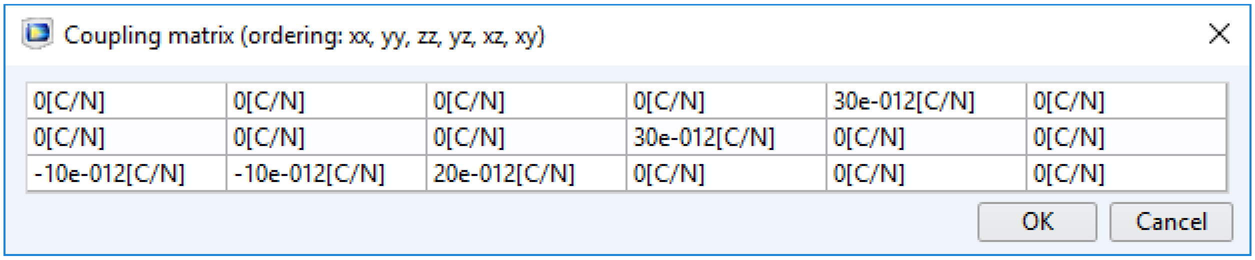

0[C/N]	0[C/N]	0[C/N]	0[C/N]	30e-012[C/N]	0[C/N]
0[C/N]	0[C/N]	0[C/N]	30e-012[C/N]	0[C/N]	0[C/N]
-10e-012[C/N]	-10e-012[C/N]	20e-012[C/N]	0[C/N]	0[C/N]	0[C/N]

Table 6: Relative permittivity matrix for screen-printed PZT

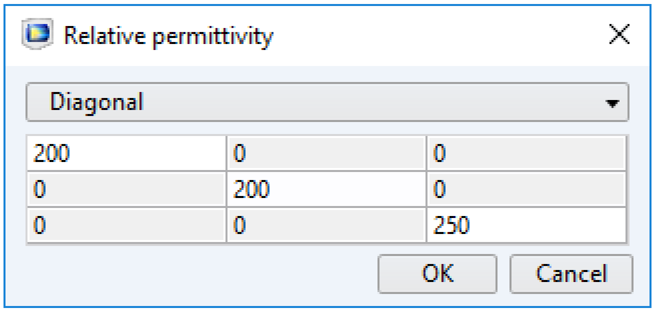

200	0	0
0	200	0
0	0	250

The COMSOL software contains several default levels of meshing. Simulations were run with increasing levels of meshing until the incremental change in the resulting eigenfrequencies was below 1%. It was determined that the “Fine” element mesh size was optimal as it provided the combination of solution convergence below the threshold and a reasonable simulation time. The meshing information for the final simulations is presented in Table 7.

Table 7: FEA Meshing Information

Number of vertex elements	258
Number of edge elements	7891
Number of boundary elements	62501
Number of elements	146059

3.3.3 Simulation

An Eigenfrequency analysis was performed using the Solid Mechanics physics to determine the fundamental frequency of the system and the associated mode shape. The fundamental frequency is 60 Hz and the corresponding mode shape is shown in Figure 18.

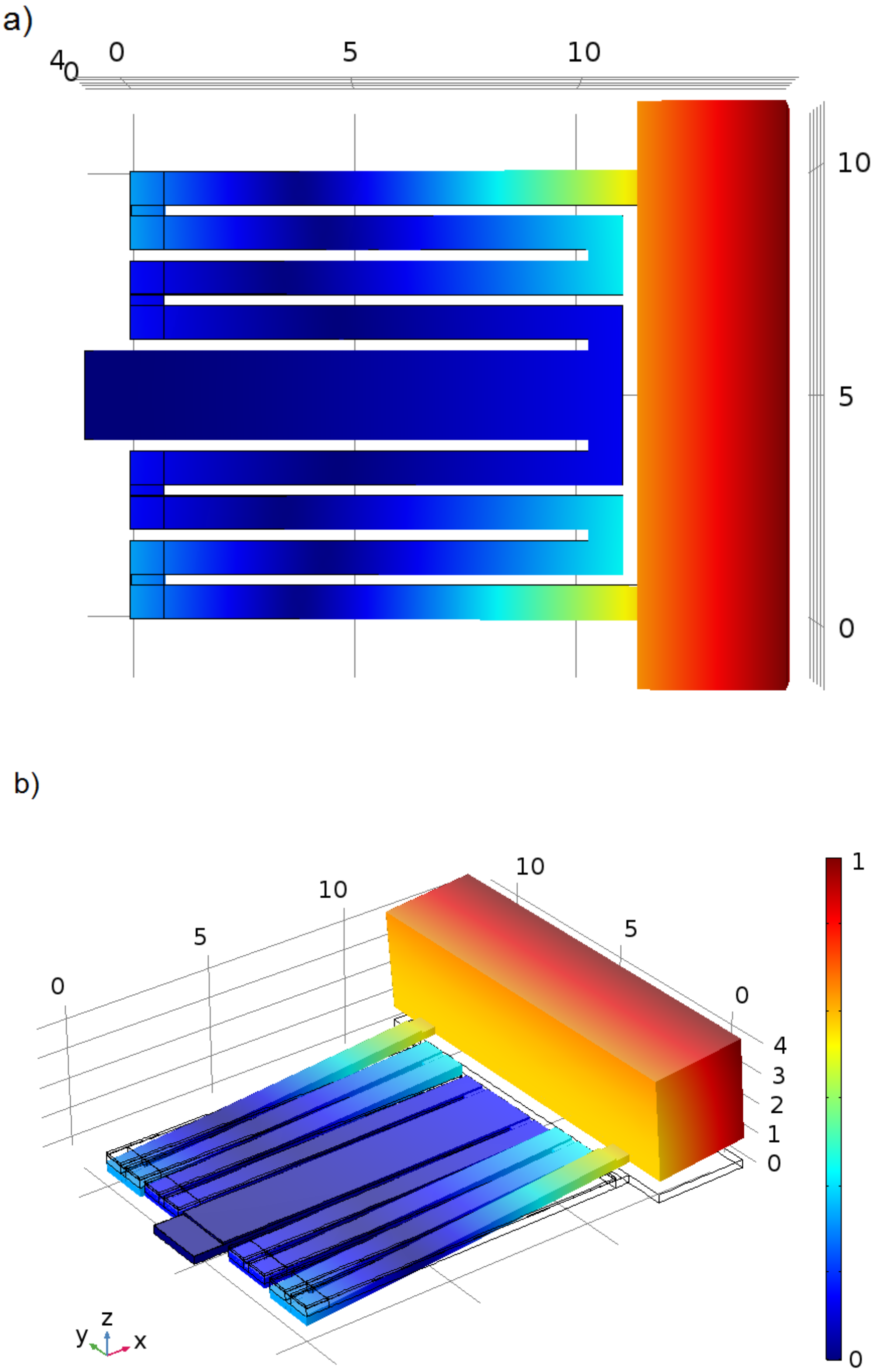

Figure 18: Fundamental mode shape showing total displacement – a) Top view b) Isometric view

The displacement mode shape shows that there is no noticeable torsional mode and that the beams of the structure experience nearly pure bending. This clearly demonstrates that the design goal of reducing torsion in the fundamental mode of the system was achieved. Furthermore, the desired resonant frequency of 60 Hz is achieved with the proposed geometry while still maintaining a small footprint.

The strain contour and piezoelectric polarization are shown in Figure 19. Areas of warm colors (red) depict tension and positive charge while cold colors (blue) show compression and negative charge.

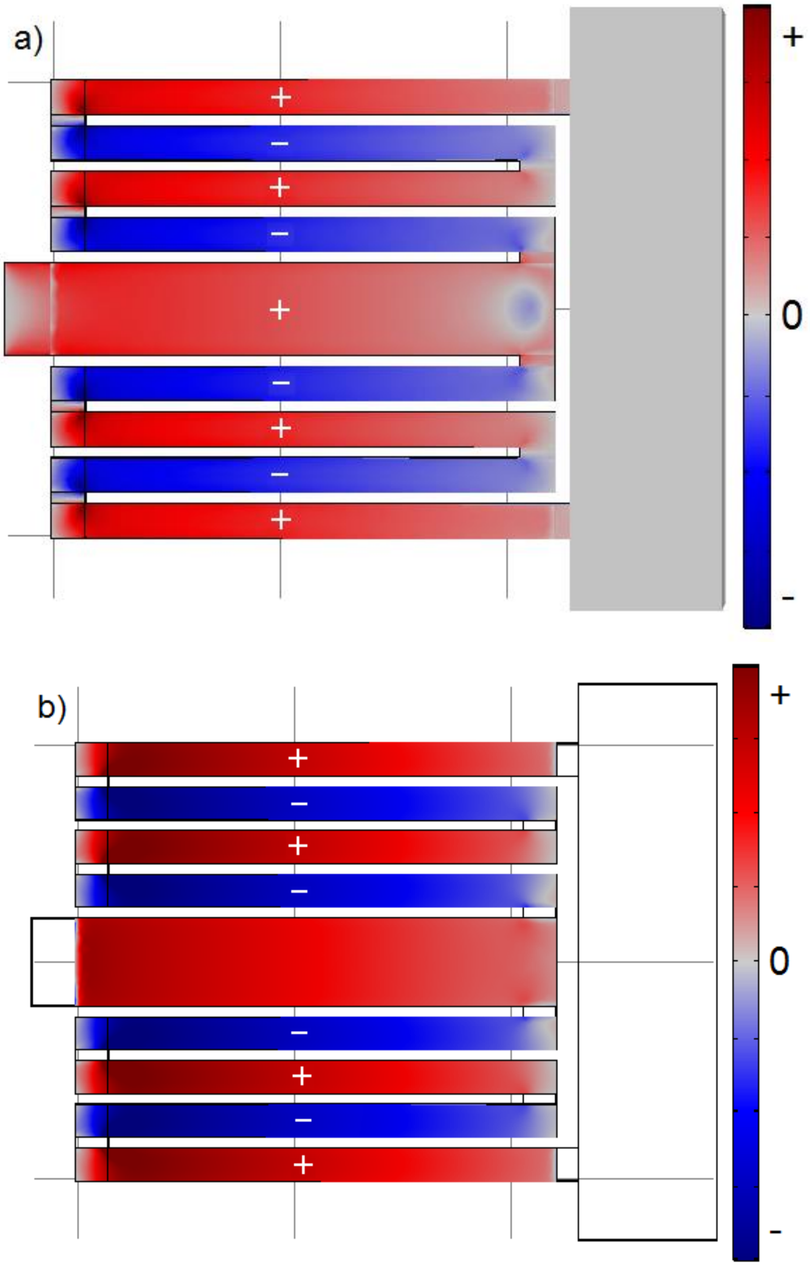

Figure 19: Fundamental mode shape a) Strain b) Piezoelectric polarization

In Figure 19a, it can be seen that each beam experiences either tension or compression along its entire length during cyclic motion. This is one of the most attractive features of the proposed design and quite critical as any strain node within the length of the beam would require segmented electrodes to avoid charge cancellation. Also, there is an alternating strain pattern seen across adjacent beams of the system. The PZT outputs a voltage according to its strain profile and therefore a continuous electrode across the entire structure cannot be used before polarization. Accordingly, the PZT has been placed along the length of each beam with disconnects at each link to avoid the strain nodes.

3.3.3.1 Frequency Domain

After determining the resonant frequency of the harvester from the Eigenfrequency study, a Frequency Domain study was performed for a frequency range about resonance. From this study certain frequency response functions (FRFs) could be generated with respect to values of importance like tip displacement and voltage or power.

Two types of excitation methods are used in the model: base excitation and tip excitation. The two methods are described below.

3.3.3.1.1 Base Excitation

A solid box was added to the base of the cantilever, as seen in Figure 20. The domain of the box was given a Prescribed Acceleration of "*g_const * acc*" in the z-direction where g_const is the gravitational constant, 9.81 m/s^2, and acc was a variable used to multiply the constant. The face of the cantilever touching the box contained a fixed constraint as done before. The results of the simulation are presented in Chapter 4 and compared to the experimental results.

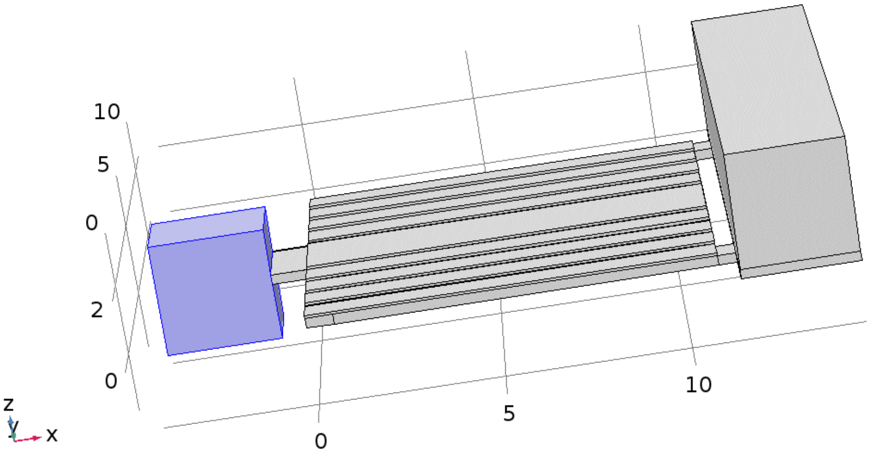

Figure 20: Base excitation model

3.3.3.2 Electromagnetic Modeling

The electromagnetic modelling is done in two parts. One 2D model contains a magnet and cross-section of a wire and is used to determine the electromagnetic force. The force is then inputted into the energy harvester model to study the response according to that electromagnetic force.

The Magnetic Fields (mf) physics is used in COMSOL to apply magnetic properties to the magnet and wire in the 2D model shown in Figure 21. A 12.7 mm long by 3.175 mm tall NdFeB magnet and an AWG10 wire with its conductor and insulation are modelled within a magnetically insulated space. A Stationary study is performed to determine the electromagnetic force.

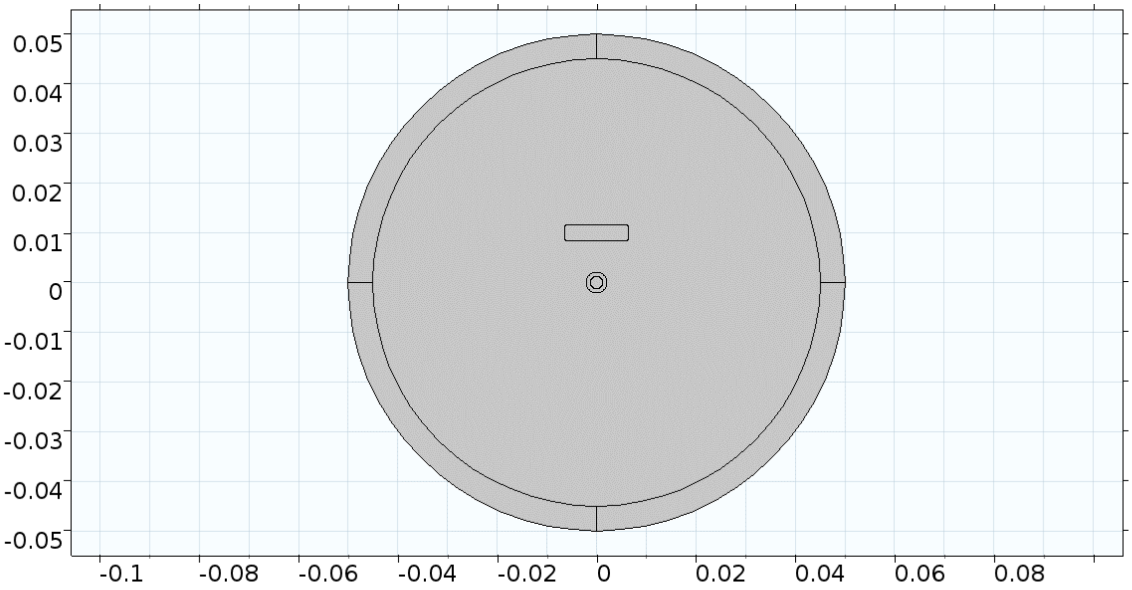

Figure 21: 2D COMSOL model of infinitely long wire and permanent magnet

As mentioned earlier, the electromagnetic force can be determined from Equation (5). A contour plot showing the gradient of the magnetic field strength of the wire with an overlay of the magnet is shown in Figure 22.

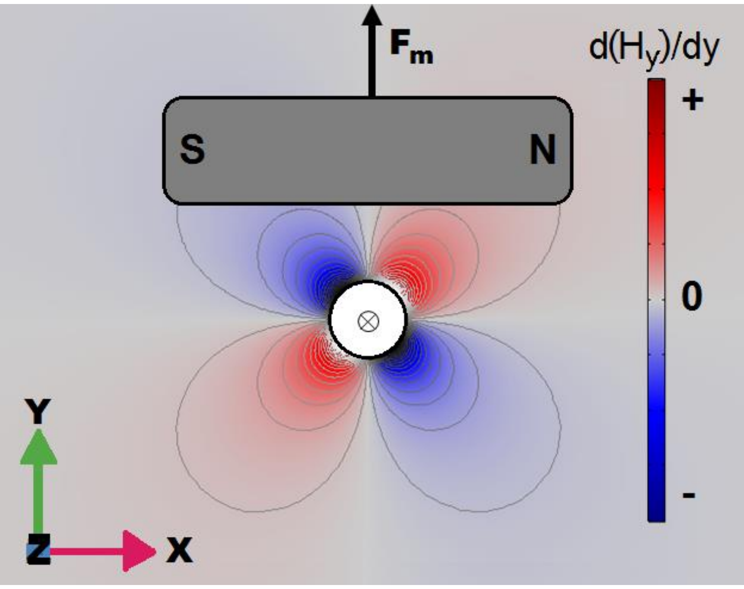

Figure 22: Permanent magnet superimposed on *d(Hy)/y* plot of a single current-carrying wire

3.3.3.2.1 Magnetic Parametric Sweeps

The electromagnetic force between the wire and magnet is a function of the geometric and magnetic parameters of both the permanent magnet and current carrying wire. Maximizing the power output of the energy harvester is an optimization problem and the parameters of the magnet should also be considered. Furthermore, the magnet needs to meet a specified mass for the resonant frequency tuning but also has size limitations due to the small volume constraints. Finally, the optimal parameters must be selected from off the shelf magnet sizes as these are known to have higher magnetic strengths. Parametric sweeps are done on the geometric properties of the magnet and current in the wire to better understand their influence on the electromagnetic force.

3.3.3.2.1.1 Varying Magnet Length

The bottom edge of the magnet is set a distance of 5 mm from the surface of the wire's insulation. A parametric study is performed on the length of the magnet and the length is swept between 5 mm and 15 mm. Figure 23 shows the vertical (y-component) of the electromagnetic force for the parametric sweep and the inset shows a contour plot of the magnetic flux density when the length is 10 mm. The graph is parabolic and suggests a maximum electromagnetic force occurs when the length is about 10 mm. Considering the 5 mm distance, this would confirm that the magnetic force is maximized when the poles of the magnet are located at 45 degree angles from the center of the magnet. Also note that the x-components of the force are zero as this component cancels out due to symmetry.

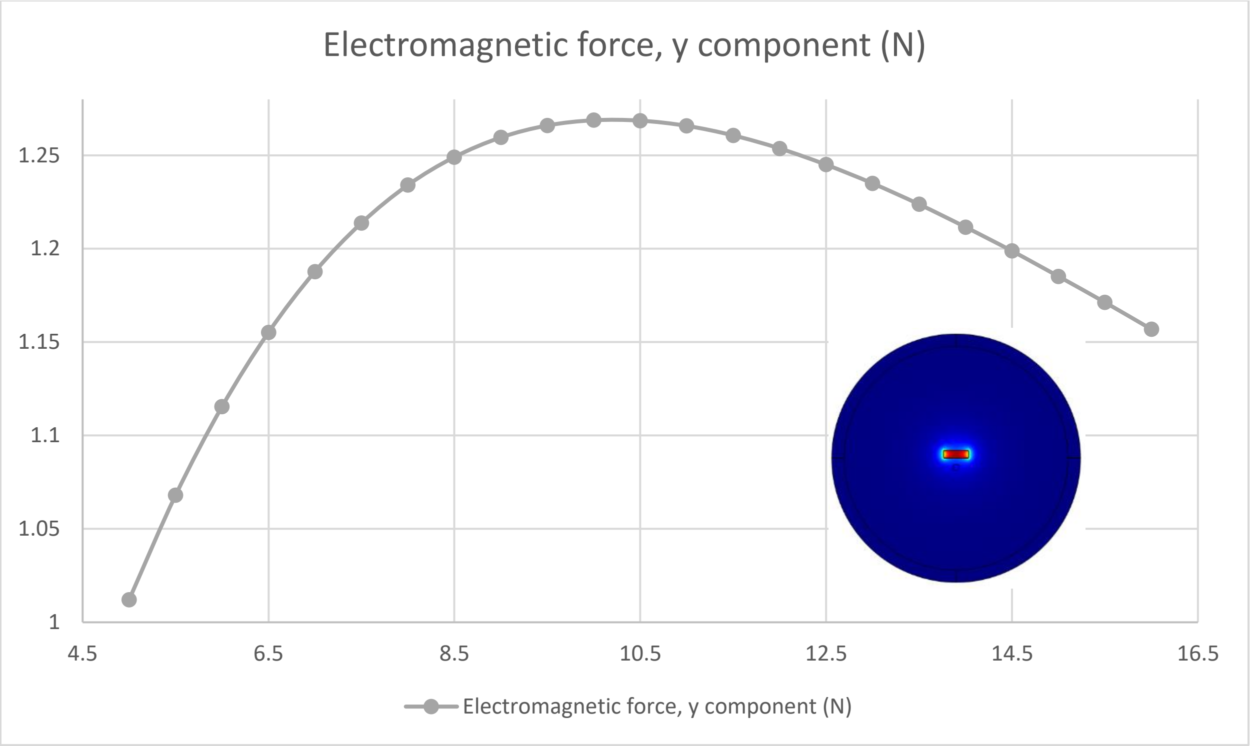

Figure 23: Electromagnetic force for varying magnet length

3.3.3.2.1.2 Varying Magnet Height

A parametric sweep on the magnet's height is performed for between 3 mm and 35 mm and the corresponding electromagnetic force is shown in Figure 24. The curve is logarithmic which suggest the change in electromagnetic force becomes less as the height is increased. Considering the size limitations, the height is typically restricted to no more than a few millimeters.

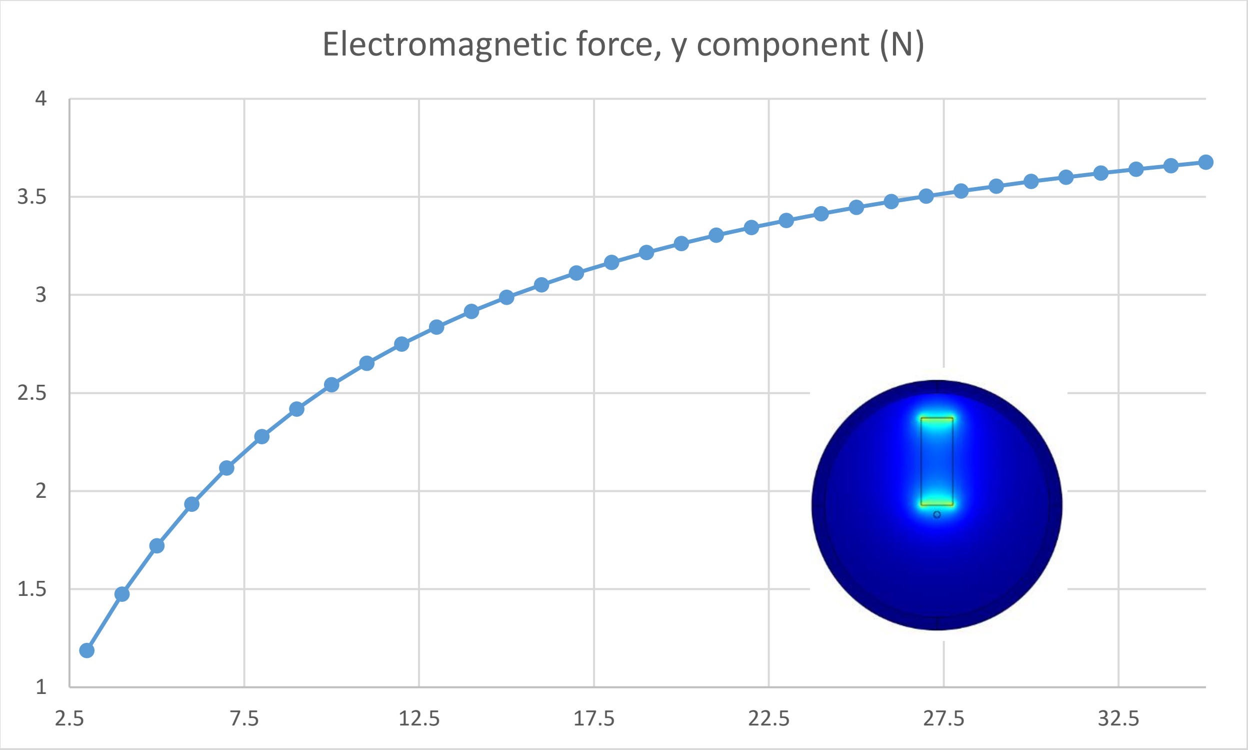

Figure 24: Electromagnetic force for varying magnet height

3.3.3.2.1.3 Varying distance between magnet and wire

The distance between the magnet and wire is varied from 0 mm to 10 mm and the resulting force is shown in Figure 25. As expected the force decays exponentially with increasing distance, and from theory we know the force is inversely proportional to the square of the distance.

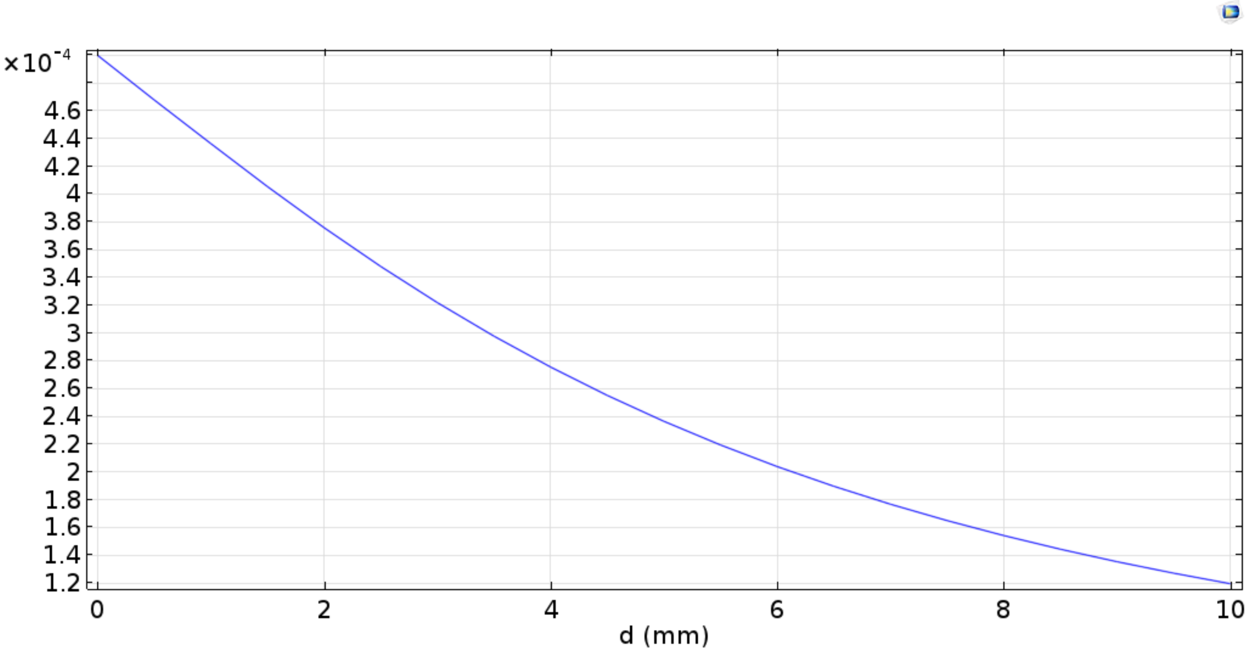

Figure 25: Electromagnetic force on the magnet vs distance between wire surface and bottom face of magnet

3.3.3.2.1.4 Varying wire current

The wire current is swept from 1 A to 10 A and studied at a distance of 9.325 mm (blue) and 6.5 mm (green) as shown in Figure 26. The electromagnetic force has a linear relation to the current in the wire and the distance between the magnet and wire affects the slope of the line; the shorter the distance the greater the slope.

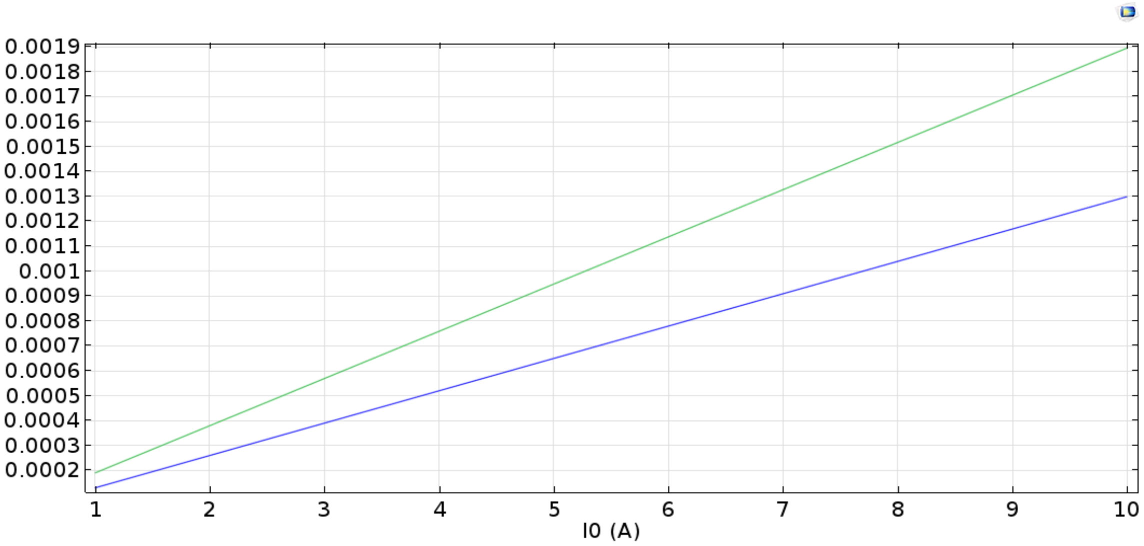

Figure 26: Electromagnetic force due to varying currents in wire. Distance = 9.3 mm (blue) and 6.8 mm (green)

3.3.3.2.2 Tip Excitation

As demonstrated from the previous section, the electromagnetic force between the magnet and wire can be calculated by specifying the geometric and magnetic properties. The electromagnetic force is determined from the 2D magnetic model and multiplied by the depth of the magnet to obtain the total volumetric force. Then the total force is inputted to the energy harvester model as a boundary load in the vertical z-direction and applied to the bottom face of the magnet, as shown in Figure 27. Although the force varies slightly as the energy harvester deflects, the calculated force is assumed to be the average. A frequency response study is performed to determine the response of the harvester due to the given inputs. The results will be discussed in the Chapter 4.

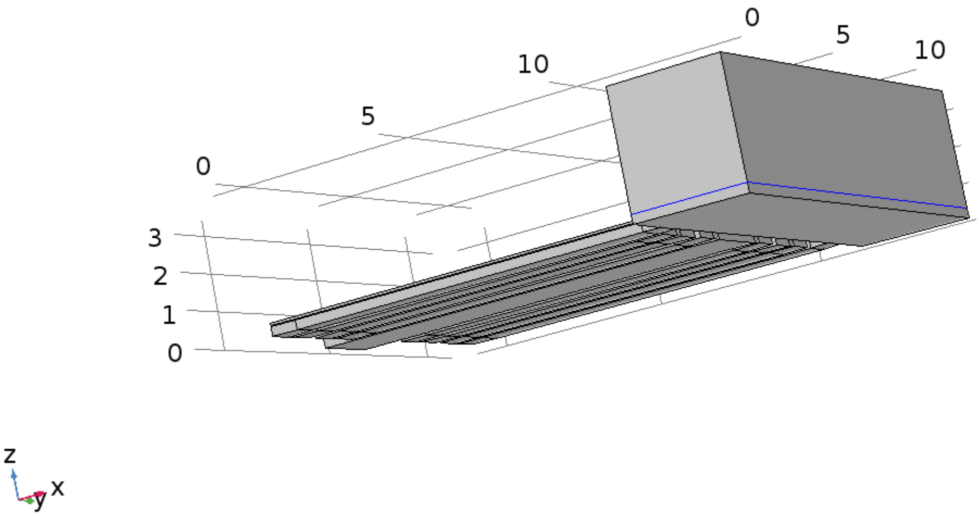

Figure 27: Inputting electromagnetic force to the energy harvester model

4 Fabrication, experimental procedure, results, and model validation

Chapter 4 presents the fabrication, experimental setup, and the test results of the MEMS piezoelectromagnetic energy harvester. The experimental results are used to verify the finite element model and observations presented in Chapter 3. The energy harvester is compared with previous works from literature. The experimental results show the proposed design results in a higher normalized power density than similar MEMS energy harvesters and is comparable to some meso-scale harvesters that use bulk PZT.

4.1 Fabrication

4.1.1 Screen-Printing Process

Screen-printing is a printing technique that uses a squeegee or blade to advance an ink over a mesh. The ink falls through the open areas in the mesh and leave an impression on the substrate below it. Figure 28 below demonstrates screen-printing [30].

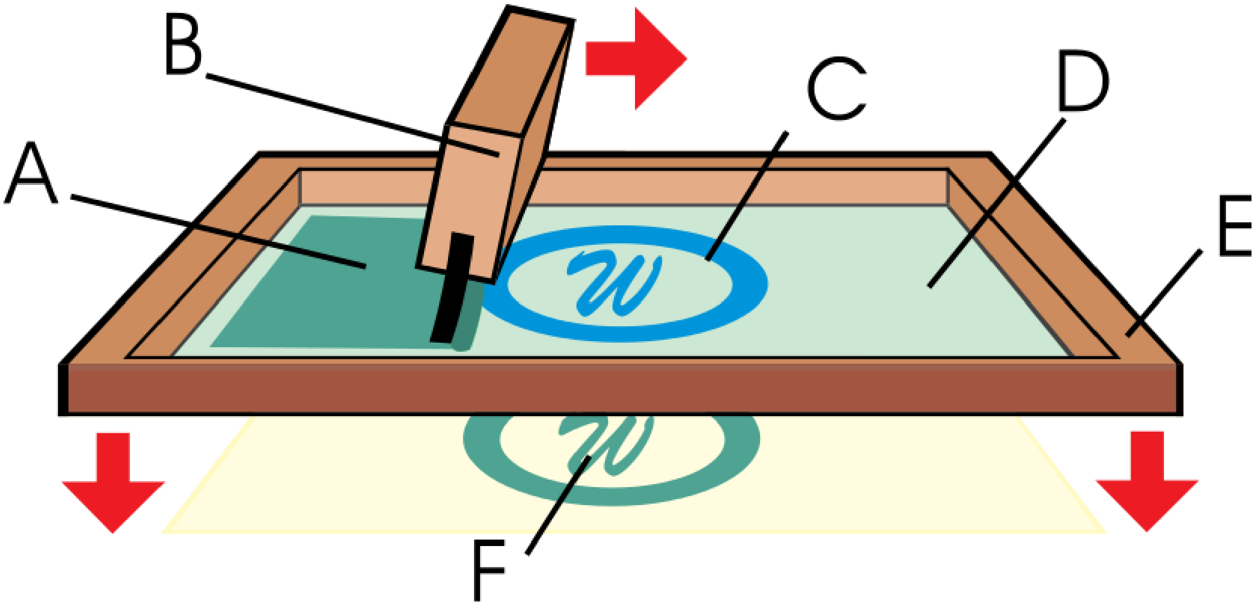

Figure 28: Screen printing A. Ink. B. Squeegee. C. Image. D. Photo-emulsion. E. Screen. F. Printed image

The printing utilizes a screen that is made out of a piece of mesh that is stretched over a frame. A stencil is formed on the screen by blocking off areas in the negative image of the design to be printed.

4.1.2 Thick Film PZT Screen-Printing Process

A piezoelectric material can also be created through screen-printing. A commercial PZT powder is mixed with other ingredients to form a PZT ink. Typically, this process involves multilevel printing which results in the PZT ink being sandwiched between two conductive inks that act as electrodes. After each deposition the unit is placed in a furnace to dry the ink and after the final layer the unit is fired to make the layers solid. The process is summarized below:

1. Print bottom electrode then dry for 20 mins at 120°C

2. Print PZT then dry for 20 mins at 120°C

3. Print top electrode then dry for 20 mins at 120°C

4. Place unit in hyperbaric chamber and expose to 100 MPa of isostatic pressure for 1 minute

5. Co-firing for two hours at 900°C

6. Poling the PZT at the Curie temperature (~280°C) at a voltage of 0.250 kV for 10 minutes under nitrogen

4.1.3 Masks and Screens

Several masks were used to create the screens to be used for each layer of printing (Figure 29). Every mask contains a dot in each of the four corners that the printer detects and uses for alignment in printing. This allows for multiple levels of ink to be printed on top of each other perfectly. The masks used in the fabrication are shown below. Figure 30 shows the completed screen for the PZT deposition.

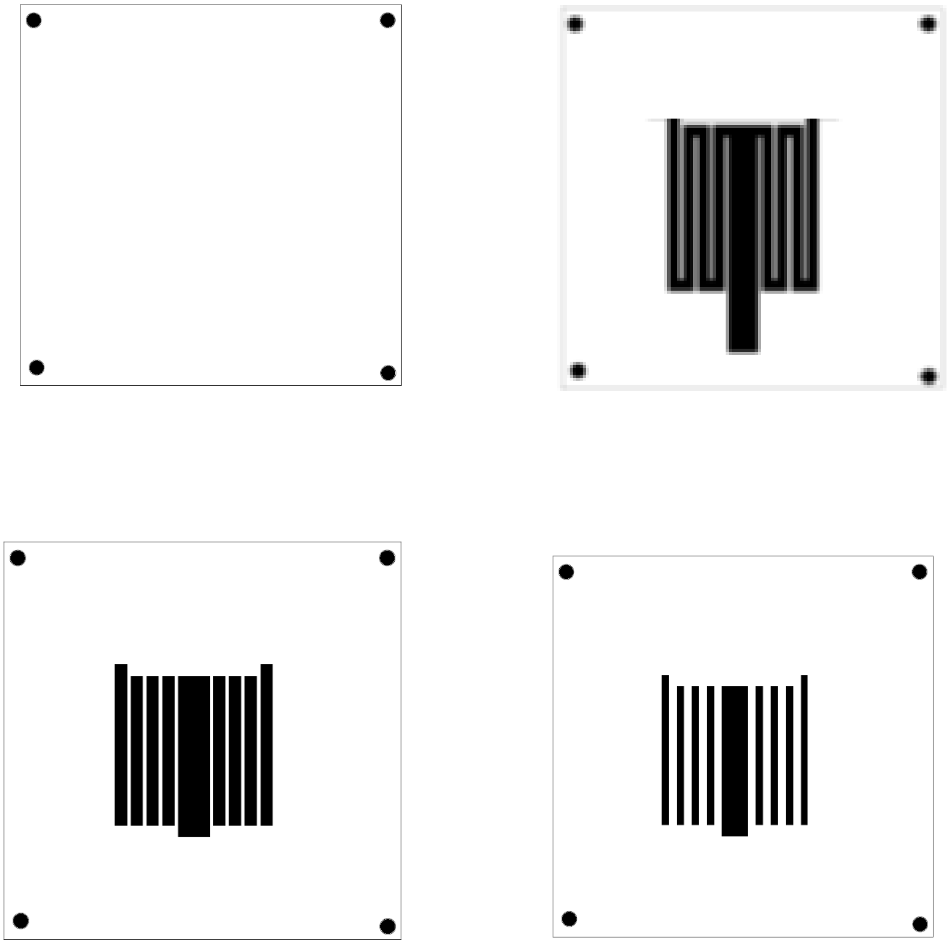

Figure 29: Masks (blank, bottom electrode, PZT, top electrode)

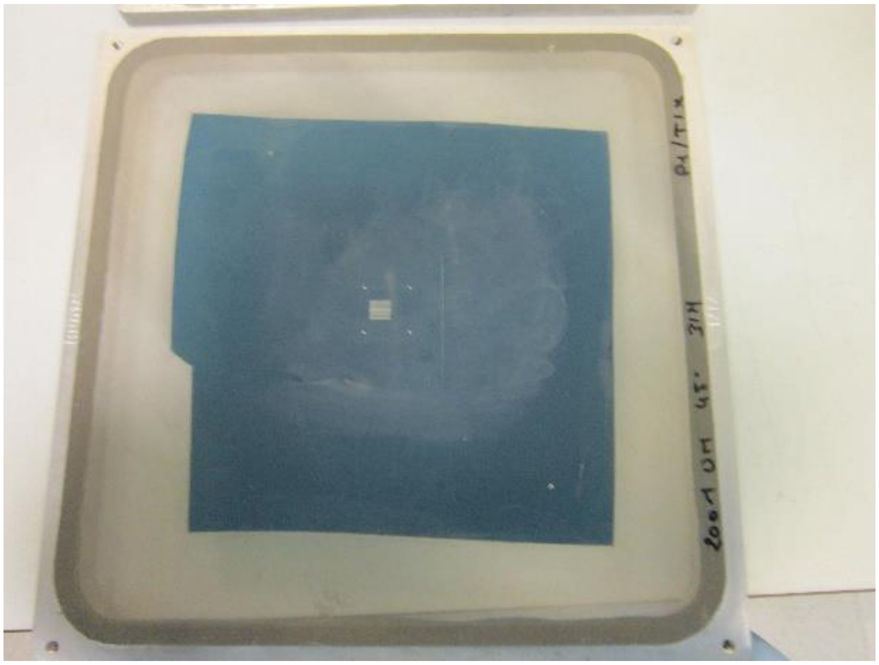

Figure 30: PZT Screen

4.1.4 Fabrication Process

The fabrication of these EHs was completed at the IMS facilities at the University of Bordeaux using a DEK screen-printer, seen below in Figure 31 [31].

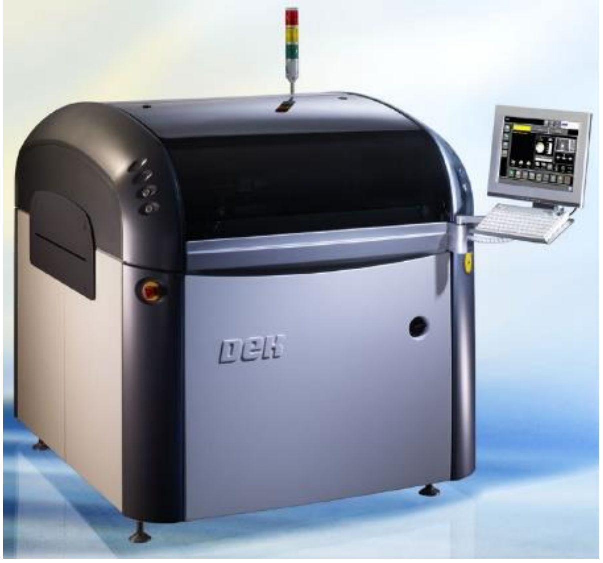

Figure 31: DEK Screen-printer

The printing process was similar to the one described earlier.

Before any printing can be a done, a substrate must be prepared to support the piezoelectric materials. The chosen substrate material is 301 stainless steel (SS) with a thickness of 254 µm and was laser cut according to the design geometry. The SS was selected for its compatibility with the firing temperature required by the screen-printable process and for its low Young's Modulus of 193GPa. The gold ink used for the electrode layer is commercially available (ESL8836 from ElectroScience Laboratories), whereas the PZT is prepared at the IMS laboratory at the University of Bordeaux. The piezoelectric paste is prepared from a commercial piezoelectric PZT powder (PZ26 from Ferroperm) mixed with 3wt% LBCu (25wt% Li2CO3, 40wt% Bi2O3, 35%wt CuO), blended with ESL4000 organic vehicle from ElectroScience Laboratories [26].

After aligning the substrate for printing, the bottom electrode is printed, dried for 20 minutes at 120°C then fired for 10 minutes at 850°C. Next, a layer of PZT and its top electrode are printed successively, and dried for 20 minutes at 120°C between each deposition. Then, the dried samples are isostatically pressed for one minute at 40 MPa to improve the densification of the layers. Afterwards, the samples are fired for 2 hours at 900°C in air atmosphere. Figure 32 shows a picture of the unit after each stage of the printing process. Figure 33 shows the fabricated unit after firing and the cross-section of the unit.

Figure 32: Each step of screen-printing process

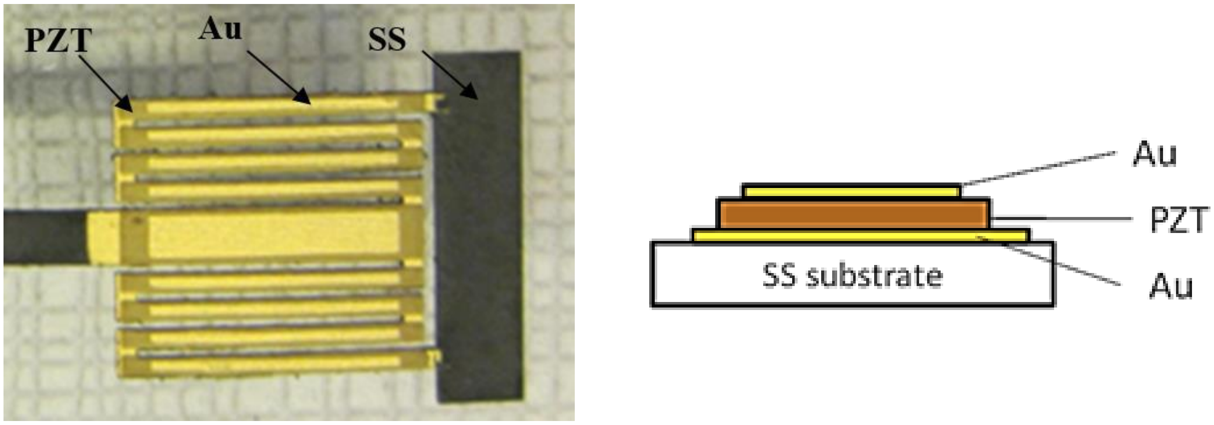

Figure 33: PZT energy harvester fabricated using screen-printing technology

An optical profiler is used to determine the overall thickness of the unit, as seen in Figure 34. Two readings are taken in the form of line A-A and B-B as shown in Figure 35b below. The A-A scan shows the variation of thickness along the length of the center beam. The B-B scan shows the variation of thickness between the beams. The results show that the densification and firing reduced the thickness of the PZT layer to approximately 55 μm. The thickness profiles of the dried Au/PZT/Au layers on the SS substrate are shown in Figure 35.

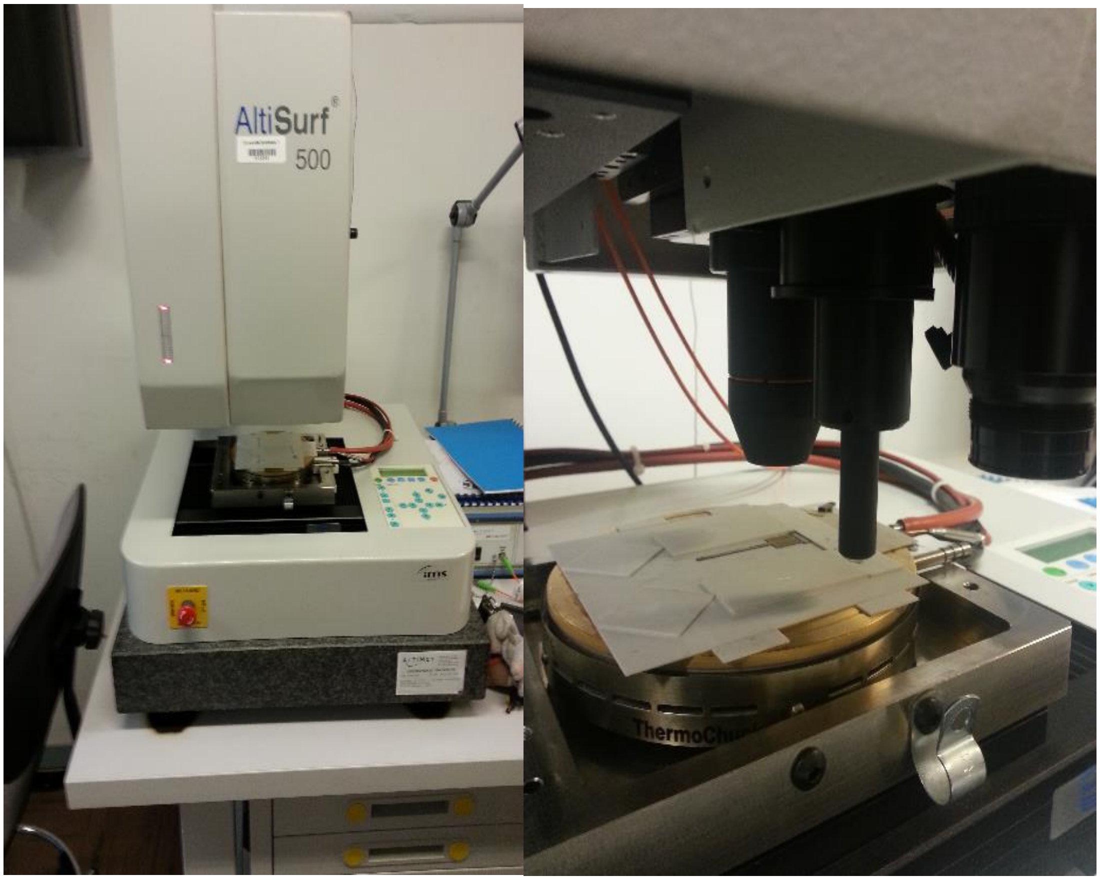

Figure 34: Optical profiler used to measure the thickness profile of the harvester

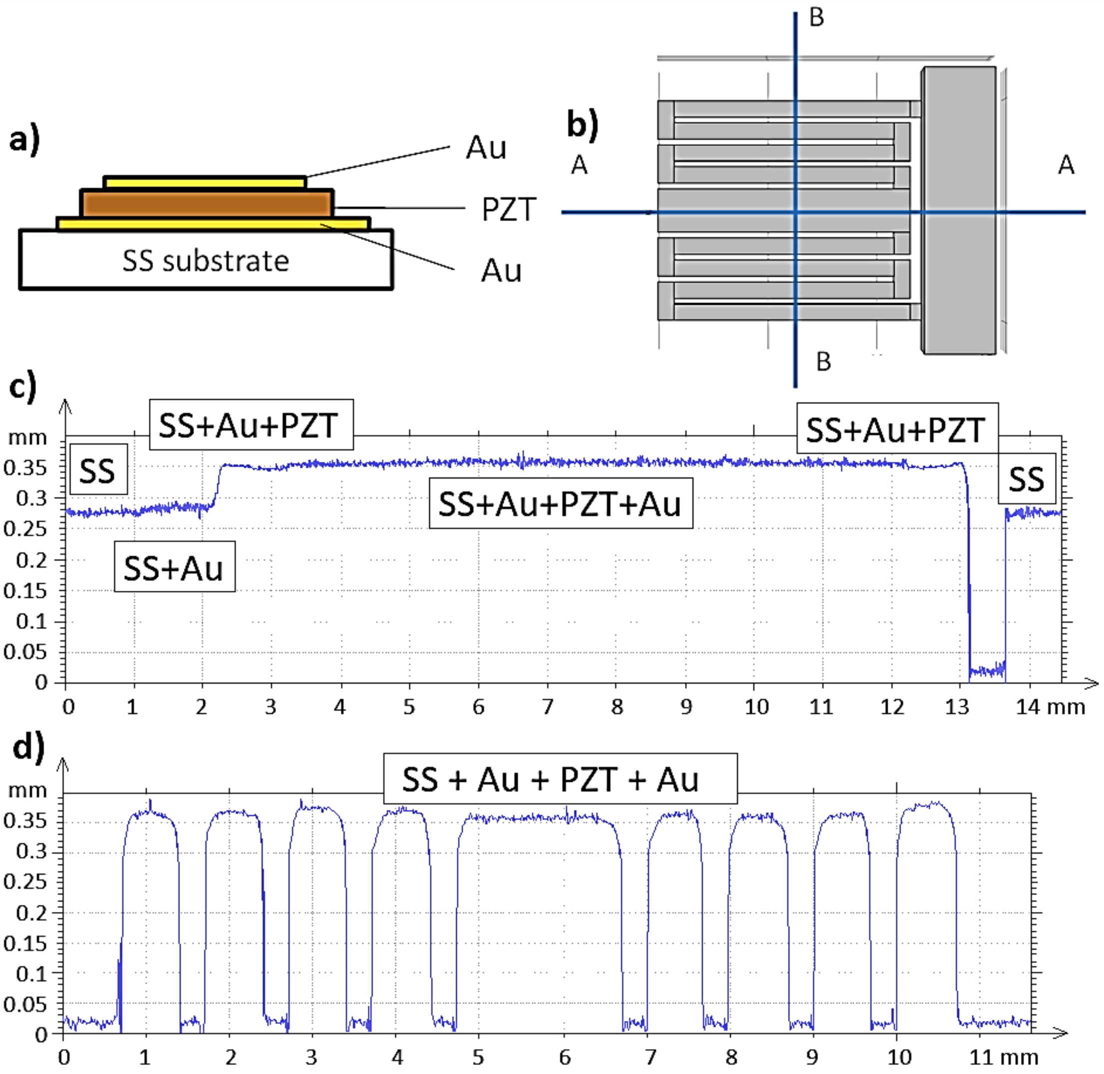

Figure 35: a) Cross section of stainless steel substrate with screen printed layers b) Thickness measurement lines across the sample for optical profiling c) Optical profile along A-A d) Optical profile along B-B

Polarization is required for the PZT layer to exhibit piezoelectric properties. Polarization of the PZT occurs close to the measured Curie temperature (~280°C) for five minutes at an electric field of 50kV/cm under a dry nitrogen environment. A strain-matched polarization (SMP) technique is used to minimize voltage cancellation across the harvester. As described in [20] the piezoelectric material of each beam is poled such that each adjacent member has the opposite poling direction. By employing this approach all of the electrodes will have the same voltage polarity. This allows for a single continuous electrode to be used across the bottom layer of the EH. A ball-bonding technique was used to make micro-wire connections between the top layers of electrodes. As a preliminary step, only four beams that experienced the same type of strain were poled.

4.1.5 Issue with fabrication and resolution

Ten units were fabricated using the procedure described earlier. The majority of the units were seen to suffer from peeling due to the adhesion between the bottom gold layer and the PZT layer. Figure 36 shows a few samples that experienced major peeling. These issues resulted in the harvesters producing lower than expected voltage output due to the reduced strain in the PZT layer. The reason for the adhesion issue was thought to be because the units were fired after the bottom gold layer was deposited. This theory was tested and the fabrication process was repeated but only one co-firing at the very end. Figure 37 showed a fabricated unit which was done by firing after all of the printing was done. The picture was taken with the aid of a microscope camera and shows the details of the micro-wiring. These units were tested under electromagnetic tip excitation, as described in the later section, and were found to be satisfactory.

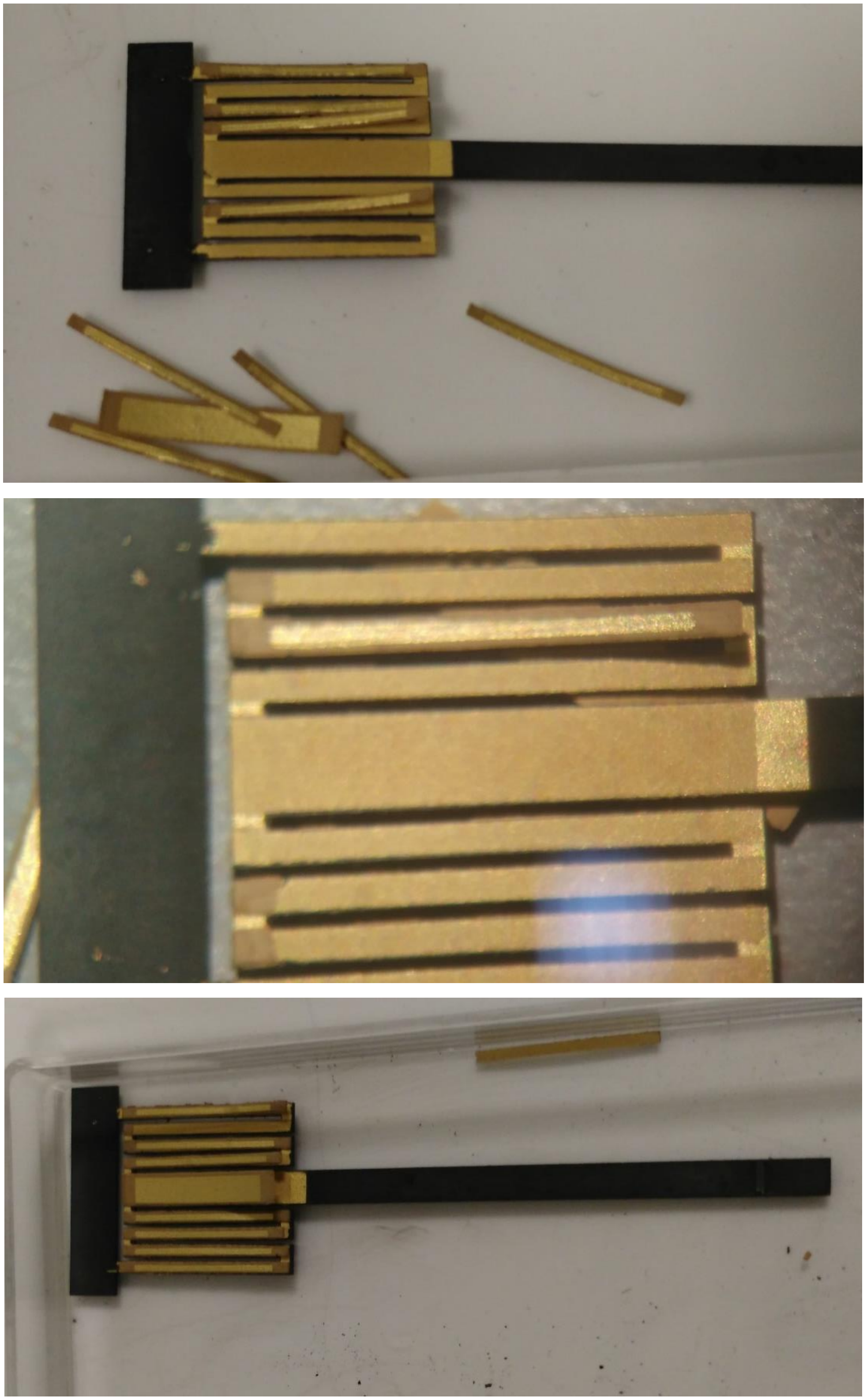

Figure 36: Peeling of layers in fabricated units

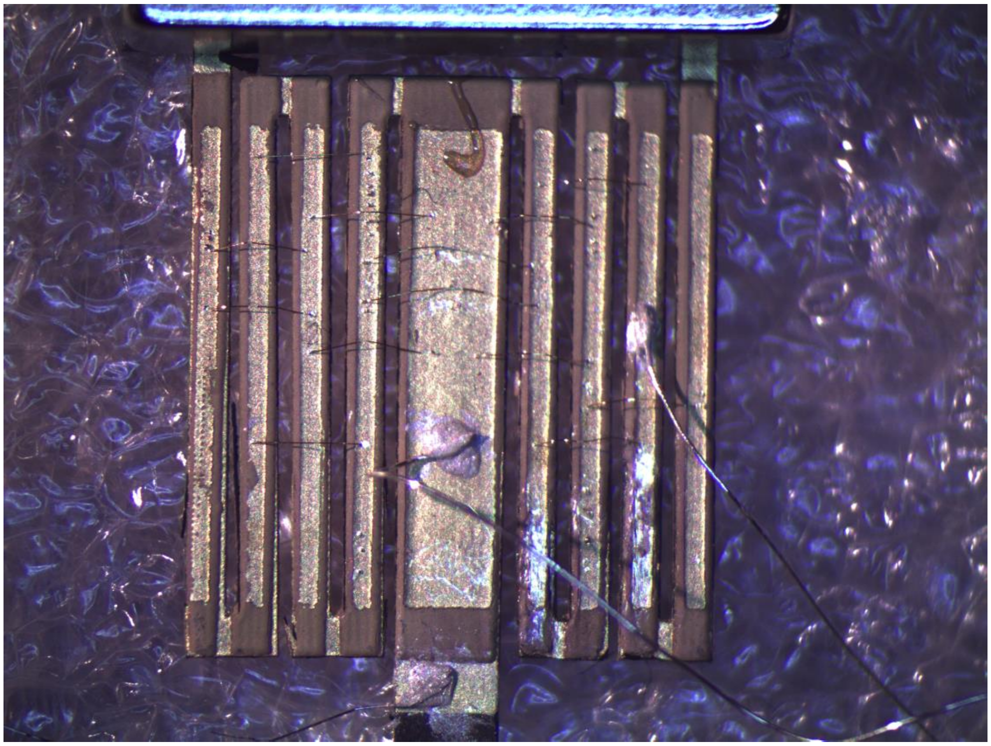

Figure 37: Fabricated unit using one firing at very end

4.2 Experimental procedure, results, and model validation

4.2.1 Experimental Methodology

The approach to experimentally validate the energy harvester comes in two parts. The first involves the experimental electromechanical testing on a shaker to validate the parameters of the stainless steel, screen-printed PZT, and neodymium magnet used in the COMSOL model. The tip displacement and voltage output will be obtained and compared against the simulated results. An electrodynamic shaker is used for base excitation and will be discussed in the following section. Once the harvester is completely characterized for base excitation conditions, it is relocated and tested under an EMF tip excitation in the form of a constant current amplitude sine sweep signal. Again the tip displacement and voltage output will be obtained but will be used to validate the electromagnetic force between the wire and magnet. The testing will be done at a series of distances between the wire and magnet and with varying currents. A load sweep will also be performed to determine the optimal load resistance for maximum power output.

4.2.2 Experimental setup and equipment

Figure 38 shows the test setup used to obtain the displacement and voltage frequency response functions of the energy harvester. As mentioned earlier, an electrodynamic shaker is used to excite the energy harvester under base excitation. The shaker used is the Modal Shop 2075 Dual Purpose shaker that can provide up to 334 N of force [32]. The shaker is mounted to the floor using a standard trunnion mounting base that is set to the vertical position. The armature of the shaker has a 25.4 mm stroke that can drive up to thousands of Hertz.

The shaker is controlled by an LMS SCADAS Mobile Data Acquisition System [33]. A laptop containing the LMS Test Lab software was connected to the LMS hardware through an Ethernet cable to measure and record experimental results in real time, as well as control signal output parameters to the shaker. This system has 8 input ports that can be configured for measurement (displacement, acceleration, voltage, current, etc.) or control feedback and 2 output ports that can be configured to provide various signals (sine, burst, etc.) The signal is fed into a linear power amplifier (Modal Shop Model 2050E09) which then drives the shaker. An accelerometer is mounted to the shaker to provide controlled feedback to the system over a range of frequencies. The accelerometer used is a PCB Piezotronics [34] model 352A24 with a sensitivity of 100.9 mV/g and can operate up to 10,000 Hz.

A laser vibrometer and controller are used to measure the displacement of the energy harvester. The sensor head is a Polytec OFV 505 with an OFV 5000 controlling unit made by Polytec [35]. The Doppler principle is used to measure the displacement of a moving object by directing a laser beam of light at the object and measuring the frequency shift of the returning light. This laser vibrometer equipment allows for production of a displacement FRF (displacement [mm]/base acceleration [m/s^2]).

BNC crocodile clamps were attached across the energy harvester to obtain the output voltage. During testing the harvester produces a sinusoidal output but the measurement obtained is the RMS voltage or the peak voltage divided by the square root of two. This measurement can be used directly to produce the voltage FRF (RMS voltage [V]/base acceleration [m/s^2]). The input resistance of the oscilloscope is 1 MΩ.

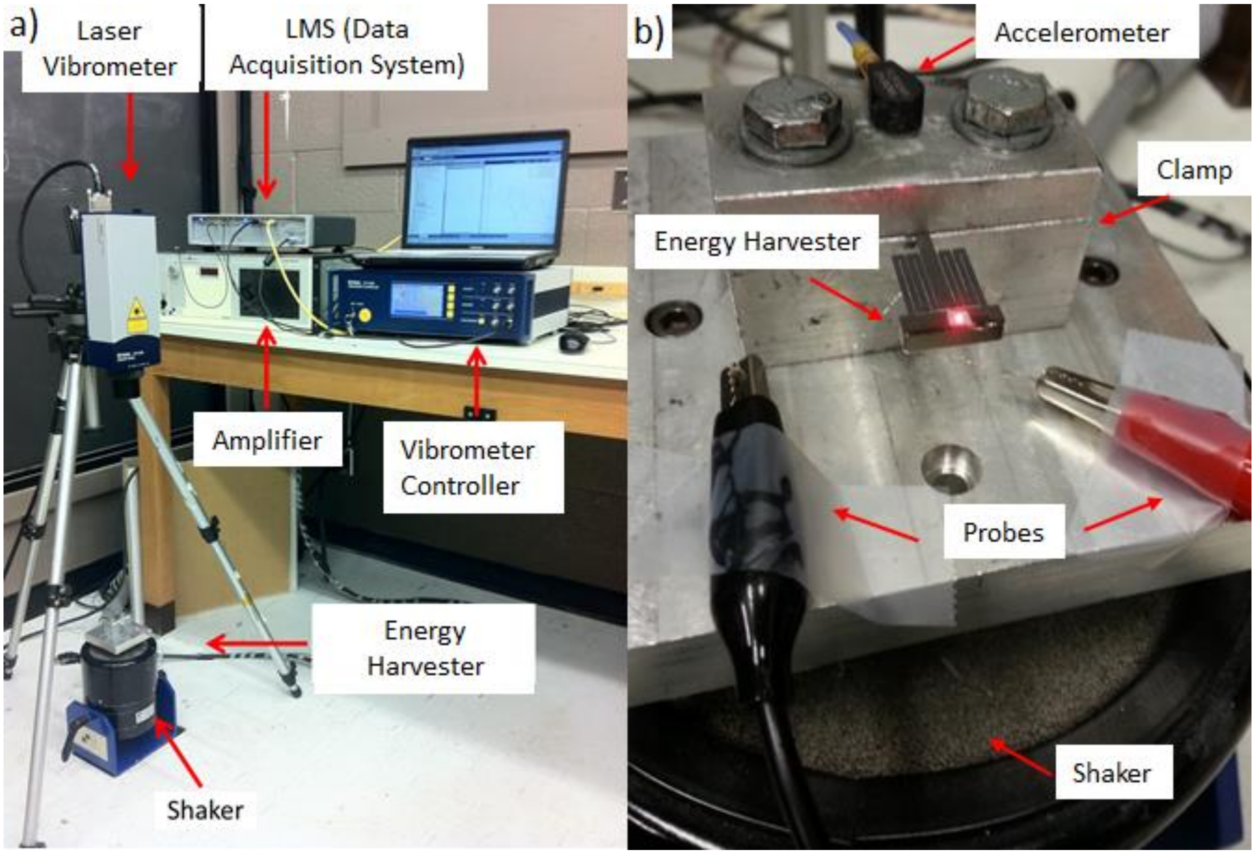

Figure 38: a) Experimental test setup equipment b) Close up of EH

4.2.3 Base excitation results

As a preliminary step, the energy harvester is tested prior to affixing the magnet. This minimizes the introduction of errors from the process of epoxying the tip magnet and provides a simpler case for comparison to the COMSOL model. An additional distance of 3 mm from the clamp is used in the experimental tests to reduce the stress experienced in the PZT near the clamp and minimize damage to the harvester. A frequency sweep from 30 Hz to 500 Hz was performed and the displacement and RMS voltage

FRFs of the experimental and simulation results are shown in Figure 39. The displacement measurement is performed at the center of the tip of the harvester.

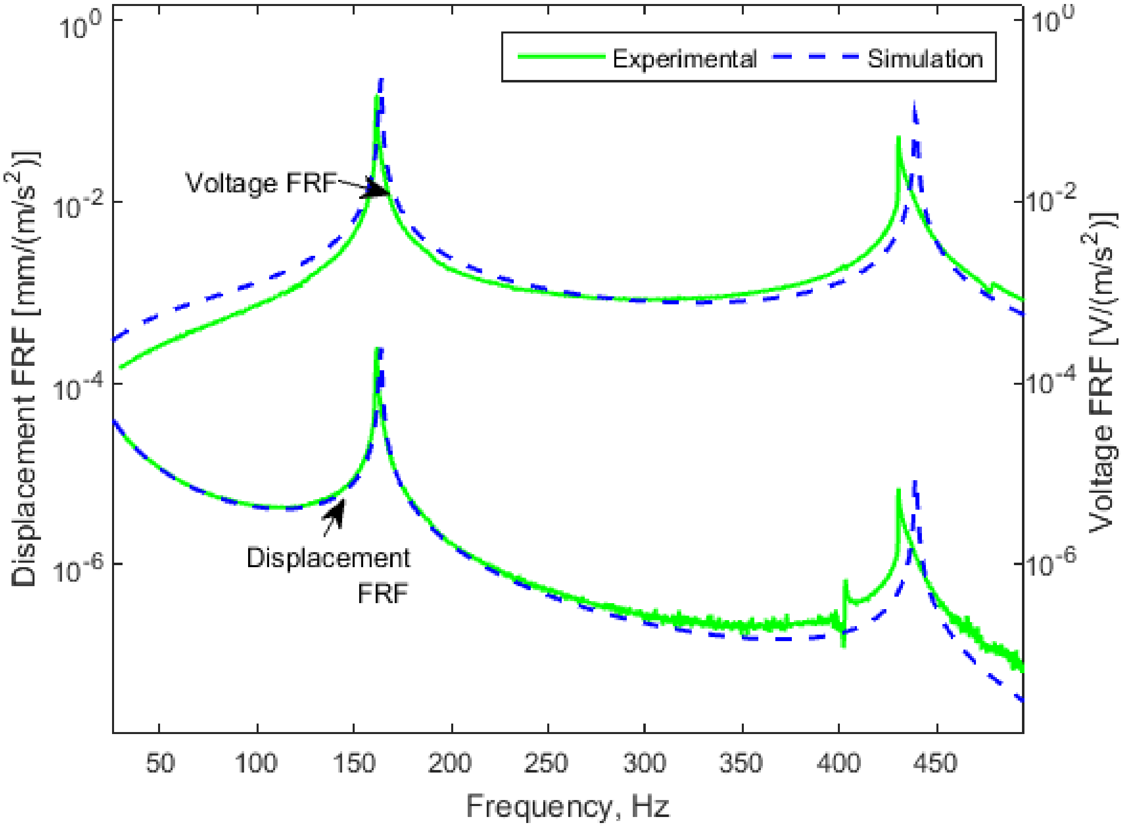

Figure 39: Displacement and voltage FRF of the EH without a tip mass

In Figure 39, the FRF presents the first three modes of vibration. Experimentally, the first two bending modes occur at 161.75 Hz and 430.5 Hz, and the first torsional mode occurs at 403.25 Hz. COMSOL predicts the first two bending modes at 163.61 Hz and 439.38 Hz, errors of 1.1% and 2.1%, respectively. COMSOL predicts the first torsional mode at 401.24 Hz, an error of 0.5%. Also in Figure 6 there is a strong correlation in the amplitudes for both the displacement and voltage FRFs when comparing experimental and simulation results. This agreement shows great confidence in the COMSOL model and it can be used in the future to optimize the geometry for greater power output.

The torsional mode for the COMSOL model does not appear in the displacement FRF of Figure 39 because the sensing point is chosen exactly in the center of the tip mass area. Due to symmetry the torsional mode is not seen at this centerline. The torsional mode in the experimental displacement FRF is an indication of two errors introduced into the system. First is that the energy harvester was not perfectly perpendicular to the clamp, and second is the laser's sensing point was not exactly at the center of the tip mass.

For the second round of testing, the magnetic tip mass is epoxied to the harvester and the displacement and voltage FRFs are obtained. Considering the good match in results with the EH without a tip mass only the fundamental frequency is of interest for the second round of testing since the fundamental frequency provides the greatest power output from the energy harvester. The experimental FRFs are presented in Figure 40.

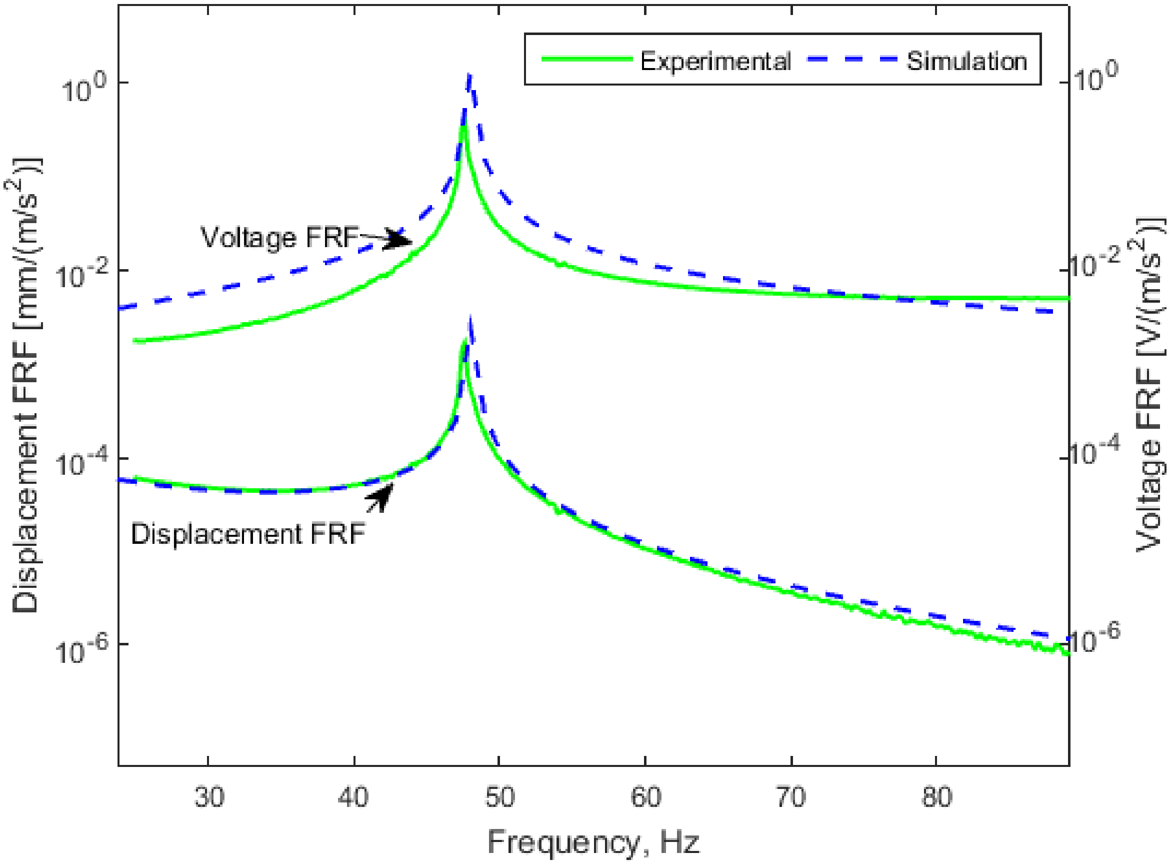

Figure 40: Displacement and voltage FRF of the EH with a tip mass

In Figure 40 the experimental fundamental frequency is measured to be 47.6 Hz and the COMSOL result is 48.1 Hz, an error of 1%. Furthermore, the amplitudes of the displacement FRFs match very well. This indicates that the COMSOL model accurately predicts the mechanical behavior of the proposed energy harvester design. Next, Figure 40 shows that COMSOL overestimated the RMS voltage of the system when compared to the experimental FRF. This difference in voltage output can be attributed to the PZT since it is the only electromechanical component of the harvester. Closer inspection of the unit showed some of the PZT had peeled off due to fatigue of the adhesion between the substrate and the PZT. The reduction in adhesion would have produced less strain in the PZT and therefore less voltage. This may have resulted from the fabrication process and also due to fatigue from testing. An additional harvester is fabricated and tested to determine if the voltage FRF results were a result of poor modelling or due to quality issues with the unit. That testing is shown in the next section.

Finally, the experimental fundamental frequency of 47.6 Hz being smaller than the design requirement 60 Hz is due to the additional 3 mm distance from the clamp, which was done to minimize damage to the unit. The difference in frequency is also attributed to the final PZT thickness being less than the designed thickness, but was fixed with the next fabricated unit. Since the PZT thickness was thinner than designed, both the overall stiffness and mass of the fabricated energy harvester were less than the initial design. Therefore, the experimental natural frequency being smaller than 60 Hz indicates that the reduction in PZT thickness had a greater effect on the overall stiffness of the proposed energy harvester than the mass. Furthermore, Figure 40 indicates that the amplitudes of the displacement FRFs match very well. This indicates that the COMSOL model accurately predicts the dynamic behavior of the proposed energy harvester design.

4.2.4 Electromagnetic testing and results

4.2.4.1 *Experimental setup*

The piezoelectromagnetic energy harvester was experimentally tested to validate the results of the FEA model. The unit was mounted above a current carrying wire (10 AWG) using an acrylic base and 1.5 mm thick spacers to control the distance between the magnet and the wire. The vertical distance between the magnet and wire was measured using a plastic caliper with an uncertainty of 1 mm. An LMS SCADAS mobile data acquisition system is used to control the current amplitude and frequency in the wire to perform a frequency sweep analysis using the Sine Control module. A Fluke i400s AC clamp is used to provide the feedback control for the system. The sinusoidal input is amplified through a Modal Shop 2050E09 power amplifier. During excitation, a Polytec OFV-505 laser vibrometer and OFV-5000 controller are used to measure the tip displacement of the harvester. The output voltage produced by the system is measured by the LMS system with an input impedance of 1 MΩ using a 10:1 probe. Any resistive load is adjusted to account for the 10 MΩ input resistance. The frequency resolution of the data acquisition is 0.01 Hz. The experimental test setup is shown in Figure 41 and Figure 42.

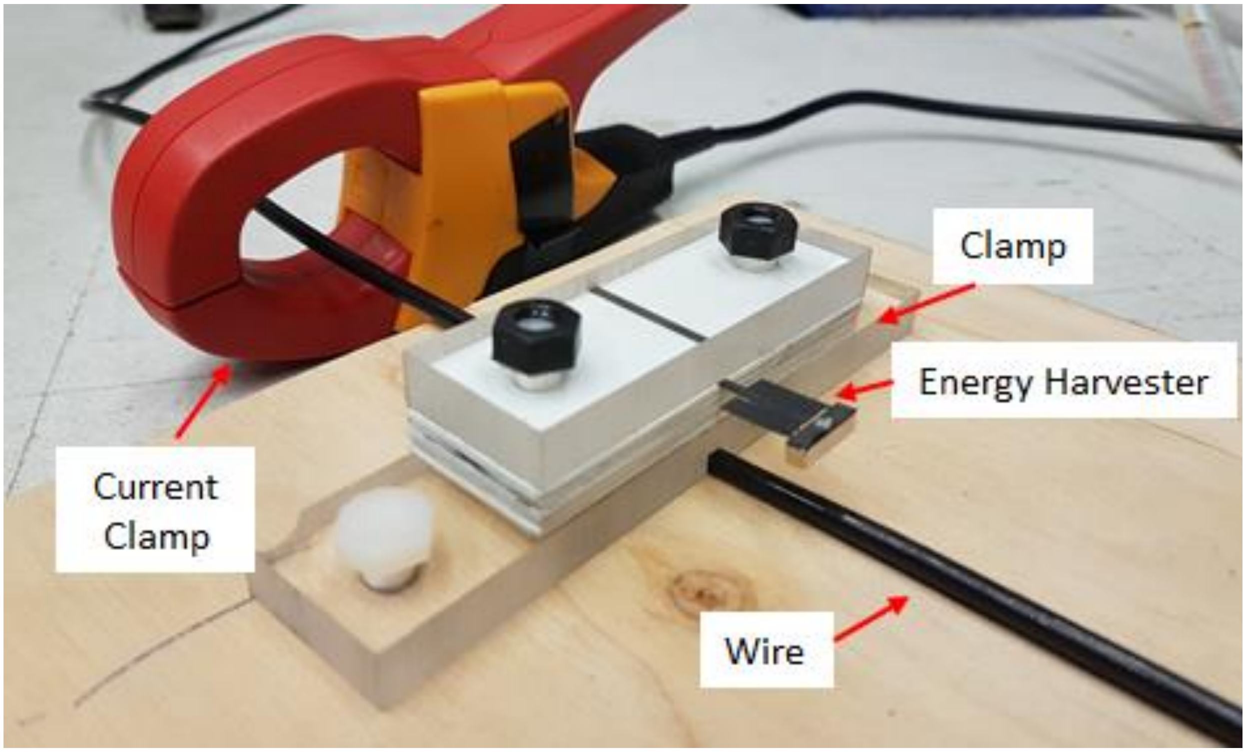

Figure 41: Piezoelectromagnetic energy harvester clamped above a current-conducting wire

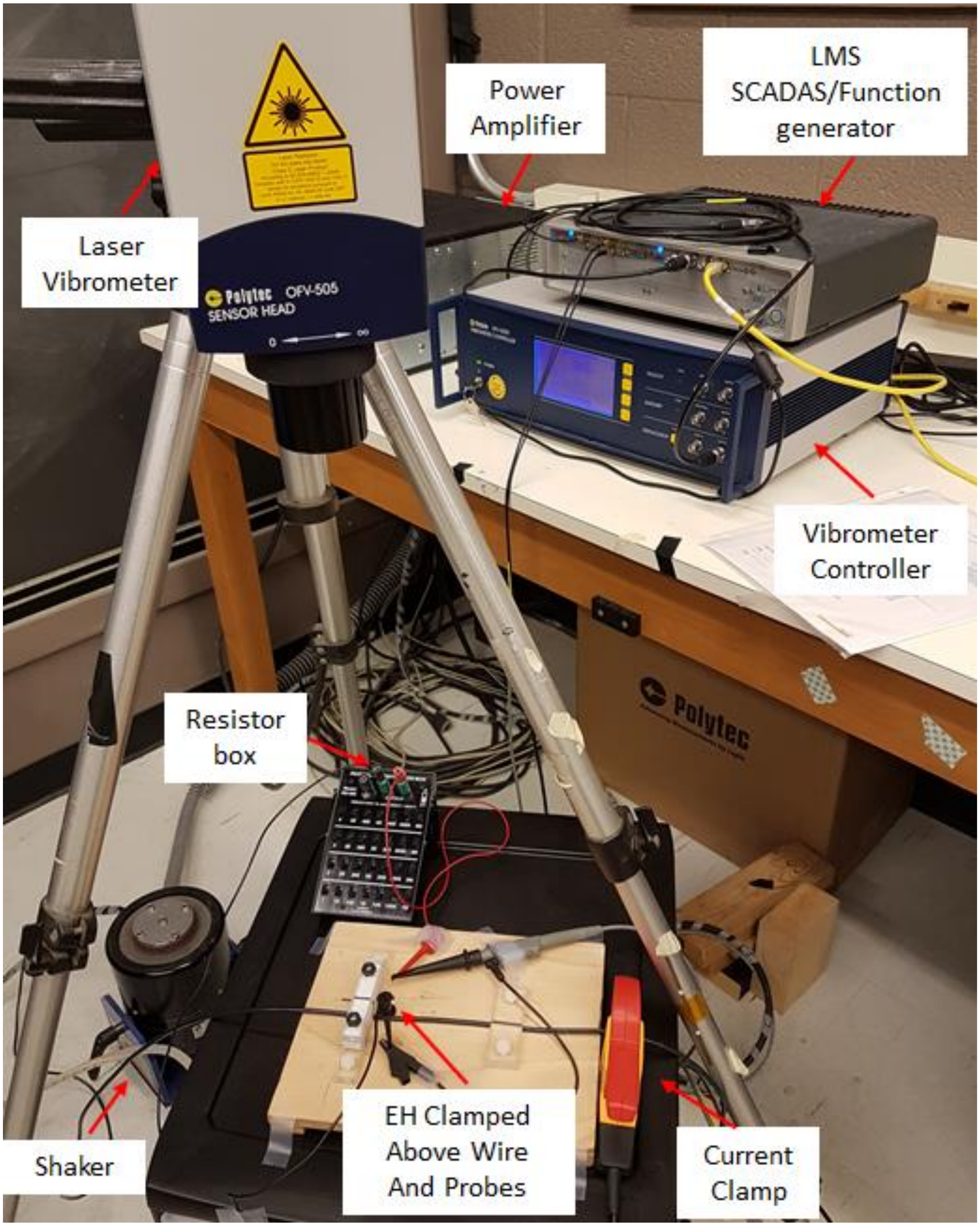

Figure 42: Experimental test setup of the piezoelectromagnetic energy harvester on a current-conducting wire

4.2.4.2 *Displacement and voltage FRF*

The harvester was initially tested with a relatively low input force (both low current and high distance to wire) to minimize the presence of non-linear effects. The harvester was mounted above the wire at a distance of approximately 12.5 mm between the bottom of the magnet and the top surface of the wire carrying a 1 A current. The experimental and simulated tip displacement and open-circuit voltage frequency response functions (FRF) are shown in Figure 43.

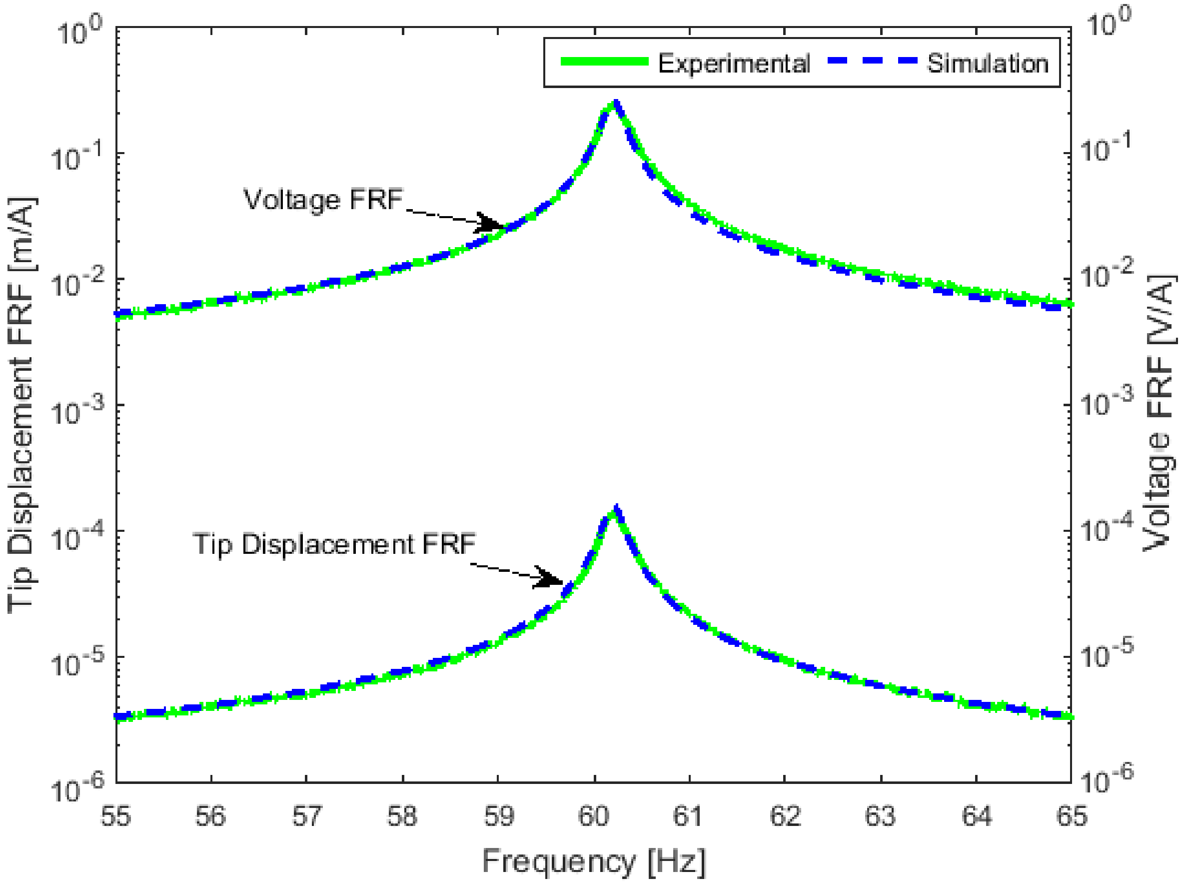

Figure 43: Tip displacement and voltage FRF showing a resonant frequency at 60.3 Hz

The experimental and simulated results show a strong agreement in both the amplitude and resonant frequency. This indicates that the COMSOL model accurately predicts the dynamic behavior of the proposed energy harvester design and the electromagnetic forces involved. The experimental resonant frequency was found to be 60.3 Hz that is suitable for harvesting from the North American power grid. The COMSOL model predicted a resonant frequency of 60.2 Hz that shows a negligible error. The damping ratio is calculated by using the quadrature peak picking method [36] and identifying the half power (-3dB) points of the voltage FRF. The damping was found to be approximately 0.0027 from the test results and applied to the COMSOL model.

4.2.4.3 *Load sweep*

Next, the energy harvester is tested with resistive loads of different magnitudes to determine the optimal load resulting in maximum power transfer. An Elenco resistor substitution box is used to conveniently provide the numerous resistances. The power is calculated by using the square of the measured RMS voltage across a resistor and dividing by its resistance value ($P_{ave} = V_{RMS}^2/R_{load}$). The power outputs across 10 kΩ to 1 MΩ are shown in Figure 44.

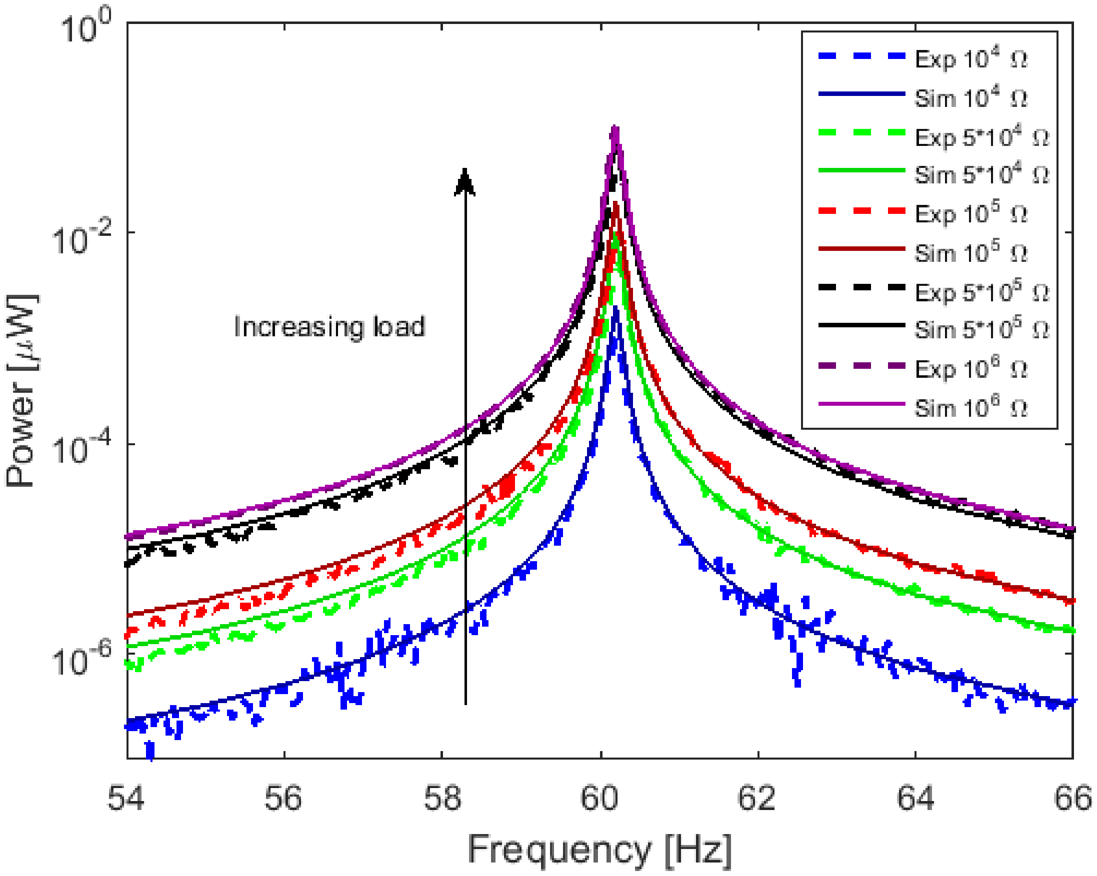

Figure 44: Power curves across 10 kΩ to 1 MΩ resistive loads

No noticeable shift in resonant frequency is seen across the load sweeps. A resistance value of 1 MΩ is seen to result in the highest power output. More resistance values around 1 MΩ are used experimentally and the peak values from each curve is used to generate the power plot shown in Figure 45 and show an optimal load range of between 1 MΩ to 2 MΩ.

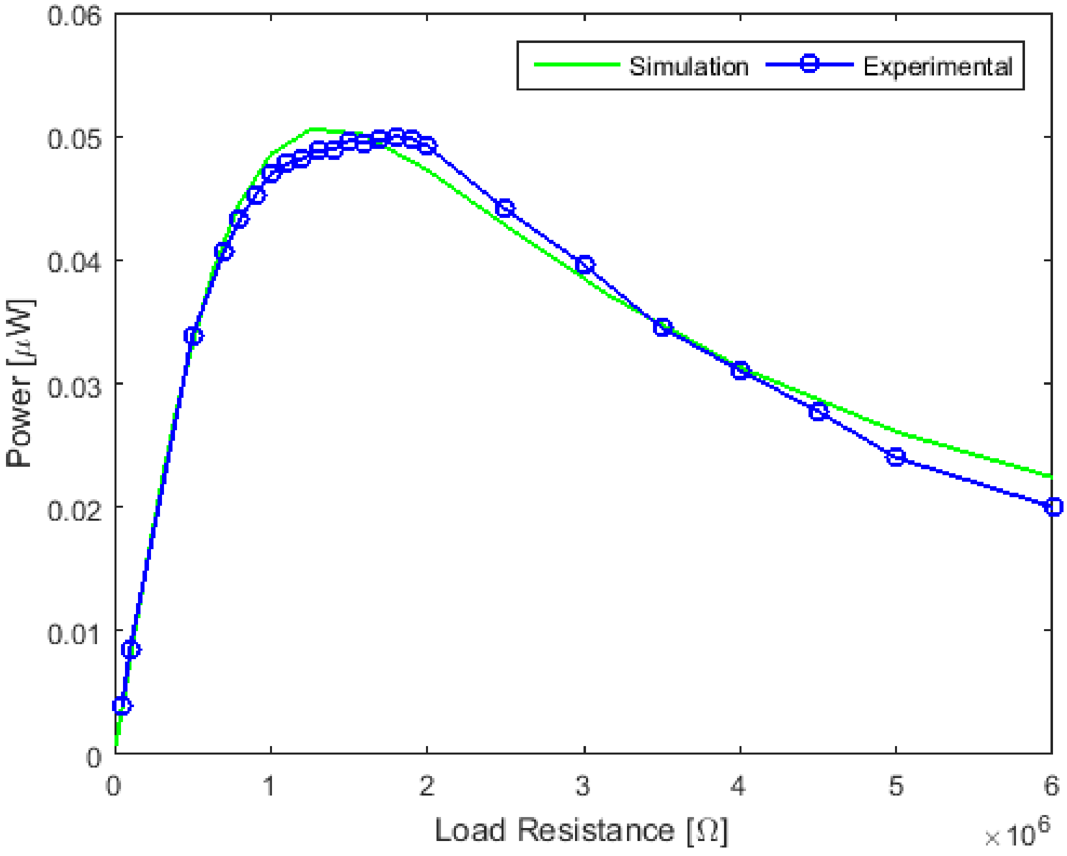

Figure 45: Power output for different load resistances

4.2.4.4 Power output vs the current in and distance to the wire

After the electromechanical model had been experimentally validated and the optimal load resistance range determined, the power outputs were measured using various distances to the wire and various wire currents. Figure 46 shows the power output measured across a 1 MΩ resistive load as a function of current and distance to the wire for the harvester.

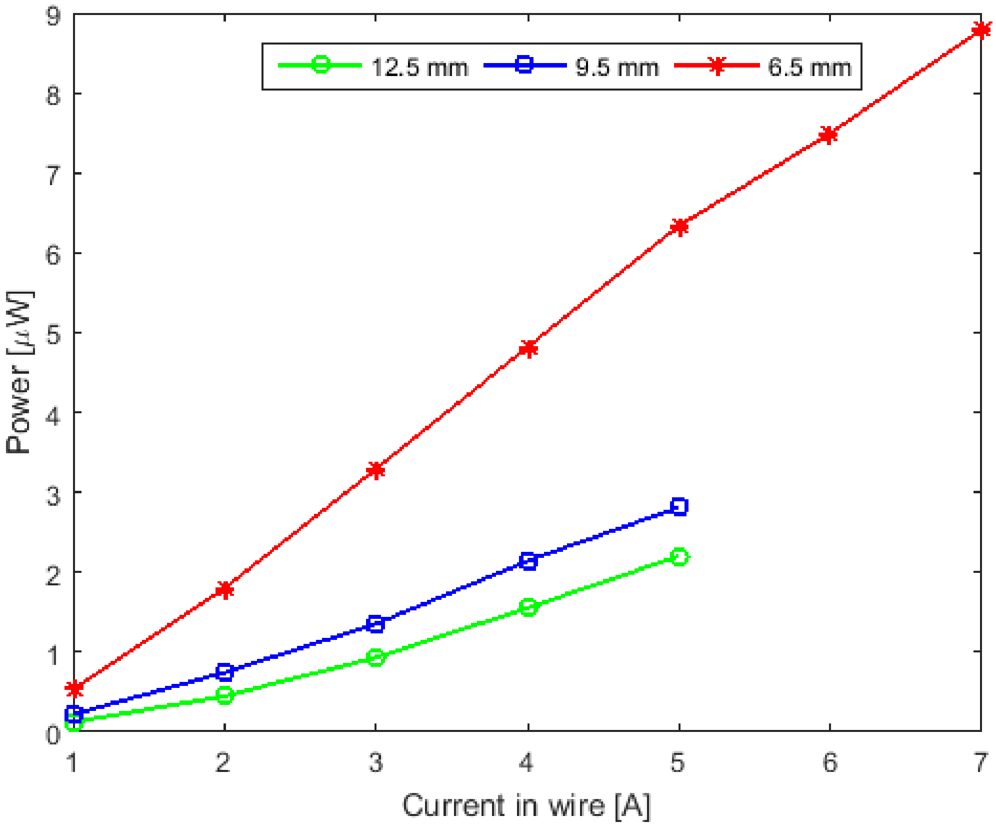

Figure 46: Power output as a function of electric current and distance from wire for the optimal load

It is shown that at a distance of approximately 6.5 mm to a wire carrying a 7 A current, approximately 9 µW is dissipated across the 1 MΩ load. All three curves were fitted with a best-fit second-order polynomial line and had R^2 values greater than 0.99. Since the force on the magnet is inversely proportional to the square of the distance and the power output is proportional to the square of the force, the overall power output grows significantly as the distance between the magnet and wire are minimized. Under large forces, however, nonlinear effects become more evident and result in a lower experimental power than expected. Further tests at smaller distances and larger current values were voided to prevent damage to the unit during these vibrations.

4.2.4.5 Non-linear effects

Figure 47 shows the experimental open-circuit voltage frequency response due to increasing currents in the wire and shows that the resonant frequency decreases with increasing excitation force. The decrease is due to the non-linear behavior of the PZT under stress. The Young's modulus and quality factor decrease with increasing excitation force [37]. These results show that for a given application the input force should also be considered when trying to tune the energy harvester. Also, the higher electromagnetic forces and increased damping widen the peak response area allowing for a wider harvesting frequency bandwidth. The back-bone curve is generated by identifying the resonant peaks for each value of input wire current. The best-fit quadratic curve of all the resonant peaks for each current is shown in Figure 48. We can observe from the plot that the harvester exhibits cubic type of nonlinearity.

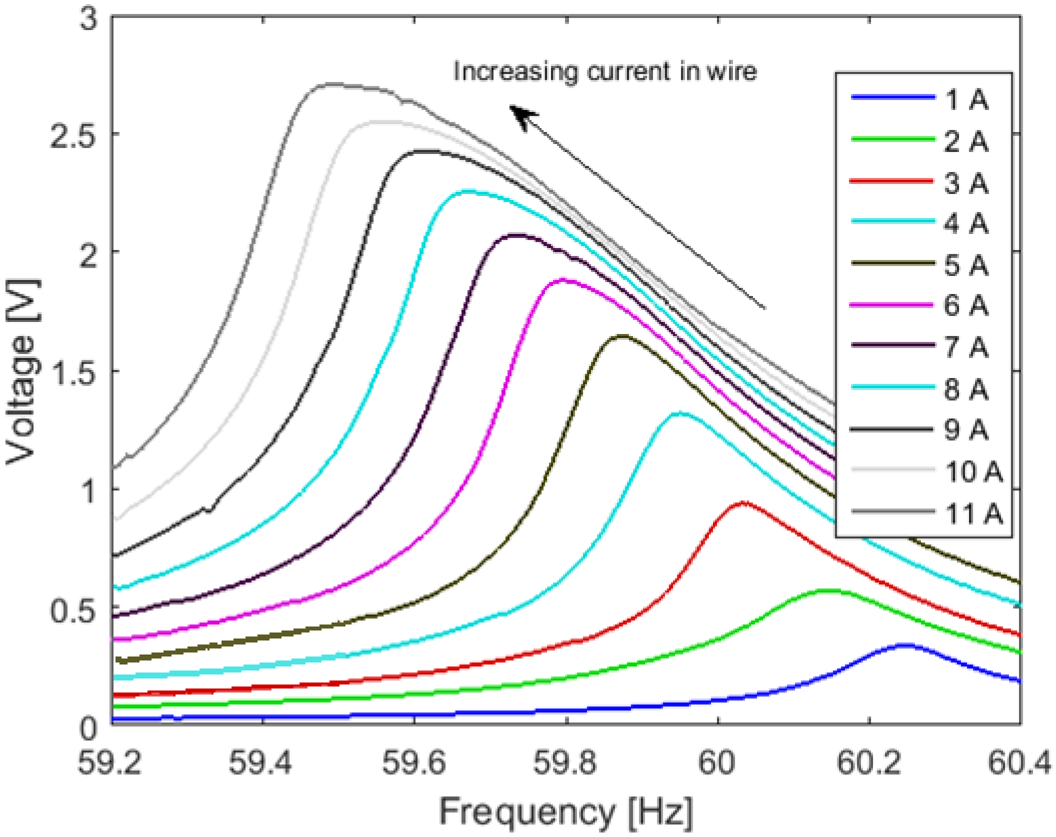

Figure 47: Voltage frequency responses for increasing wire currents demonstrating non-linear effects

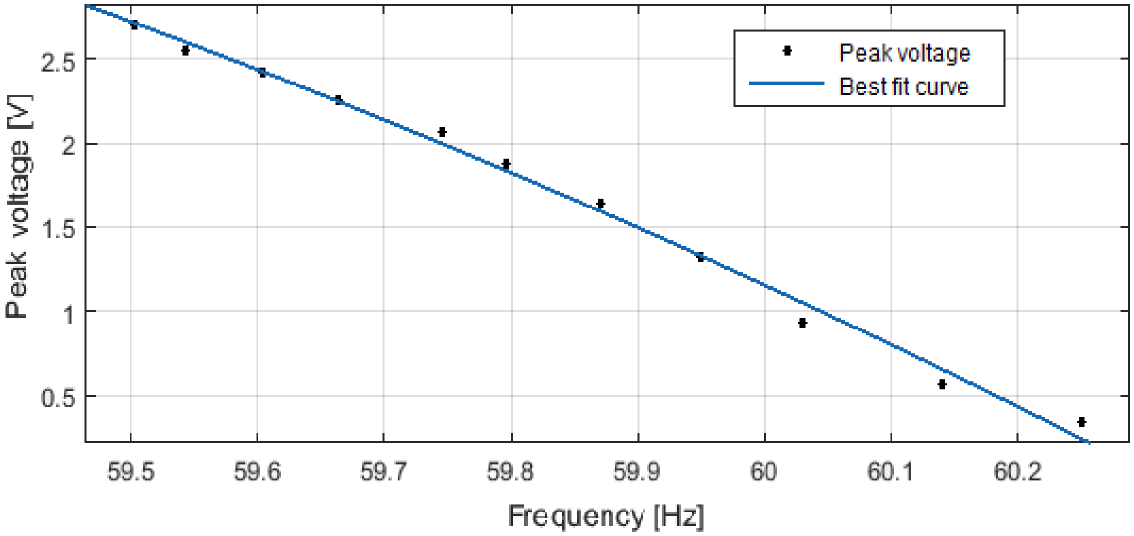

Figure 48: Backbone curve of the frequency response. Dots represent the peaks of the experimentally obtained frequency response curves and the solid line represents their best fit quadratic curve

4.2.4.6 Comparisons to other works

In this section, the results of the proposed design are compared to the previous work in the literature and presented in Table 8. As previously mentioned, the overall power output is a function of the current in the wire, the distance between the magnet and the wire, and the remanence of the magnets and, therefore, must be considered for a fair comparison. The effective volume considers the sum of the volume of all beams and magnets. The normalized power density of the piezoelectromagnetic energy harvesters is calculated by dividing the power output by both the effective volume and the magnetic force.

Table 8: Normalized power density for previous piezoelectromagnetic harvesters and the present work

Reference	**Deposition method**	**Magnet distance (mm)**	**Magnetic remanence (T)**	**Wire current (A)**	**Power output (µW)**	**Frequency (Hz)**	**Effective volume (mm^3)**	**Normalized Power Density µW/(T*A*mm)**
This work	Screen-printed PZT	6.5	1.32	7	9	60	169.7	0.242502
Paprotny [8]	Sputtered AlN	2.5*	1.32	1	2 (simulated)	57*	111.81	0.084695
Olszewski [9]	Sputtered AlN	2*	1.3	2	1.5	42.3	20.69	0.111537
Paprotny [6]	Bulk PZT	2.5	1.48	20	2,700	60	1,731.06	0.329337
Chen [38]	Bulk PZT	2	1.4*	2.5	295.3	50	1,282.74*	0.263098
He [7]	Bulk PMgN-51	4	1.45	10	566	50	265.92	2.348645

* Values interpolated from data in the referenced literature.

By comparing the normalized power densities shown in the table, one can see that the present work shows significant improvement over previous MEMS devices, [8] and [9], with a 2.9 and 2.2 times increase in the normalized power density, respectively. This improvement validates the advantages of the centrally-supported meandering geometry and the screen-printing fabrication process. The proposed geometry minimizes the number of overall strain nodes that plague other geometries. The results for the present work also shows good potential when compared to the larger scale units in [6], [38], and [7]. In addition to the larger scale for devices in [6], [38], and [7], bulk PZT is used that is known to have higher electromechanical coupling compared to the MEMS fabricated technology, and, therefore, is expected to have higher normalized power densities. As such, the benefits of the MEMS screen-printing fabrication technology remains one of the main advantages of the suggested work. However, it is seen for certain cases that the result of the proposed design is quite comparable to that of the bulk PZT units.

4.2.4.7 Test with current from wall outlet

The harvester was finally tested in a real world application. This test was achieved by using a simple 1500 W space heater that was plugged into a wall outlet. The common residential electrical outlet in a North American power grid operates at 120 VAC and has a primary harmonic at 60 Hz. The dual cord of the heater was carefully separated to isolate a single wire. The energy harvester was mounted above a single wire and the current clamp surrounded the same wire. The distance between the magnet and the wire surface was kept at 12.5 mm to keep the electromagnetic force low to prevent damage to the unit and be cautious of unexpected spikes in current.

The measurement system used was the same as before although no feedback control was used to control the current in the wire. The LMS software package Spectral Control was used and allowed for real time monitoring of the current clamp and harvester output. The heater was turned on and Figure 49 shows the current in the wire and the resulting voltage output from the harvester.

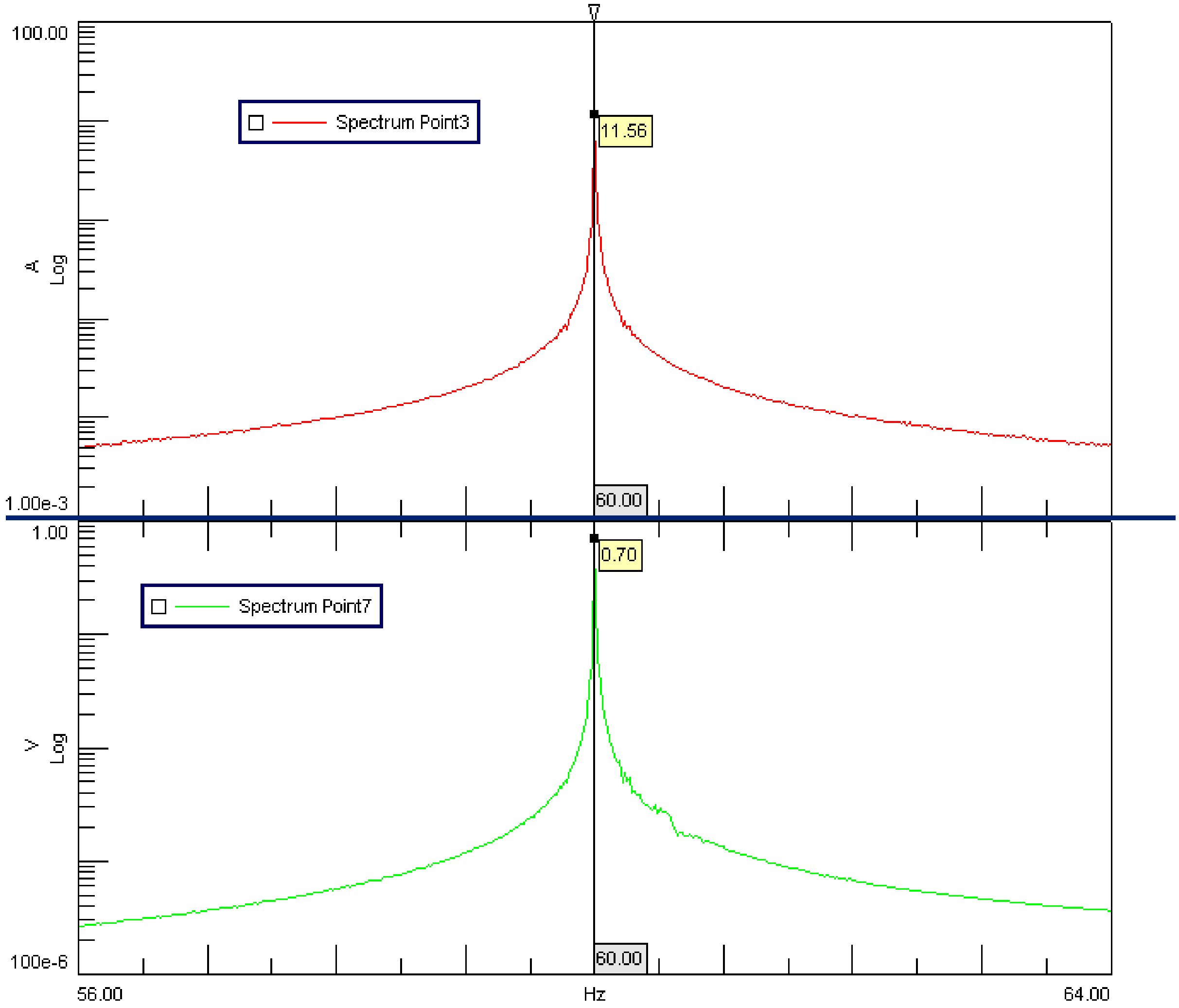

Figure 49: Current in the wire (top) and corresponding voltage output of harvester (bottom)

The maximum current output from the heater is 11.56 A at a frequency of 60 Hz. The voltage output from the harvester closely follows the shape of the wire current. Around 60.2-60.6 Hz in the voltage output there is what appears to be noise, but the resonant frequency of the harvester is known to be in this area and is likely showing transient behavior in the measurement. As the resonant frequency of the harvester did not perfectly match 60 Hz the power output was not maximized. Also, during experimental setup one of the large wires broke off the harvester and resulted in a lower output.

5 Conclusion

In summary, this manuscript documents the development of a low frequency MEMS piezoelectromagnetic harvester using fabrication techniques suitable for mass-production, resulting in a viable solution for Smart Grid applications.

5.1 Summary

A MEMS piezoelectromagnetic energy harvester has been fabricated through screen-printing of PZT on a stainless steel substrate with a centrally-supported meandering geometry. The energy harvesting device was modelled using COMSOL and validated against experimental results. Experimental data was collected by base excitation and electromagnetic tip excitation. The experimental and simulated results were in good agreement which validated the model. The design goals of a suitable footprint for microelectronic applications and a resonant frequency of 60 Hz were also achieved. It is shown that the proposed geometry experiences dominant bending when compared to the previous MEMS-based work on this technology, helps increase the power efficiency, and simplifies the electrode geometry. As a result, the present work results in an improved normalized power density compared to the previous MEMS-based piezoelectromagnetic harvesting technologies for the proposed application.

5.2 Future work

Future work will involve improving the fabrication process to provide a greater predictability of the final PZT thickness in the harvester. The polarization process should also be refined to eliminate the complicated micro-wiring. This may also reduce the overall damping of the harvester and result in a greater power output.

Long term testing of the device should be conducted to determine the impact of fatigue over time on the harvester and its power output. The limitations of the harvesters could be assessed at greater wire currents and when the unit is brought closer to the wire to see the effect of cracking. Limiting springs may be added to the prototype to prevent the unit from deflecting beyond a certain displacement and preserve the longevity of the harvester.

Moreover, with the validated COMSOL model the geometric parameters of the system may be optimized for greater power output. Finally, the unit should be combined with a current sensor, power conditioning circuitry, and wireless communication and tested as a smart grid solution.

References

[1] U.S.-Canada Power System Outage Task Force. Final report on the august 14, 2003 blackout in the united states and canada: Causes and recommendations. 2012.

[2] A. Erturk, D.J. Inman, Piezoelectric Energy Harvesting, John Wiley & Sons, 2011.

[3] S. Naifar, S. Bradai, C. Viehweger, O. Kanoun, Survey of electromagnetic and magnetoelectric vibration energy harvesters for low frequency excitation. Measurement 106 (2017) 251-263.

[4] E. Leland, P. Wright, R. White, Design of a MEMS passive, proximity-based AC electric current sensor for residential and commercial loads. Proc.PowerMEMS (2007) 77-80.

[5] E.S. Leland, R.M. White, P.K. Wright, Energy scavenging power sources for household electrical monitoring. PowerMEMS (Dec.2006) (2006) 165-168.

[6] I. Paprotny, Q. Xu, W.W. Chan, R.M. White, P.K. Wright, Electromechanical energy scavenging from current-carrying conductors. IEEE Sensors Journal 13 (2013) 190-201.

[7] W. He, P. Li, Y. Wen, J. Zhang, C. Lu, A. Yang, Energy harvesting from electric power lines employing the Halbach arrays. Review of Scientific Instruments 84 (2013) 105004.

[8] I. Paprotny, R. White, P. Wright, Modeling, design and fabrication of (10× 10× 4 mm3) MEMS AC energy scavenger for smart grid applications. PowerMEMS (2010).

[9] Olszewski OZ, Houlihan R, Mathewson A, Jackson N, A low frequency MEMS energy harvester scavenging energy from magnetic field surrounding an AC current-carrying wire, Journal of Physics: Conference Series, 2016, pp. 012039.

[10] S. Roundy, E.S. Leland, J. Baker, E. Carleton, E. Reilly, E. Lai, B. Otis, J.M. Rabaey, P.K. Wright, V. Sundararajan, Improving power output for vibration-based energy scavengers. IEEE Pervasive computing 4 (2005) 28-36.

[11] S. Roundy, P.K. Wright, J. Rabaey, A study of low level vibrations as a power source for wireless sensor nodes. Computer Communications 26 (2003) 1131-1144.

[12] N.E. Dutoit, B.L. Wardle, S. Kim, Design considerations for MEMS-scale piezoelectric mechanical vibration energy harvesters. Integrated Ferroelectrics 71 (2005) 121-160.

[13] T. Hehn, Y. Manoli, CMOS circuits for piezoelectric energy harvesters. Springer Series in Advanced Microelectronics 38 (2015) 21-40.

[14] S. Roundy, P.K. Wright, A piezoelectric vibration based generator for wireless electronics. Smart Materials and Structures 13 (2004) 1131.

[15] H. Kim, Y. Tadesse, S. Priya, D. Inman, Piezoelectric energy harvesting. Energy Harvesting Technologies 1 (2009) 3-39.

[16] W. Choi, Y. Jeon, J. Jeong, R. Sood, S. Kim, Energy harvesting MEMS device based on thin film piezoelectric cantilevers. Journal of Electroceramics 17 (2006) 543-548.

[17] M.A. Karami, B. Yardimoglu, D.J. Inman, Coupled out of plane vibrations of spiral beams for micro-scale applications. Journal of Sound and Vibration 329 (2010) 5584-5599.

[18] M. Ibrahim, A. Salehian, Modeling, fabrication, and experimental validation of hybrid piezo-magnetostrictive and piezomagnetic energy harvesting units. Journal of Intelligent Material Systems and Structures 26 (2015) 1259-1271.

[19] M.A. Karami, D.J. Inman, Analytical modeling and experimental verification of the vibrations of the zigzag microstructure for energy harvesting. Journal of Vibration and Acoustics 133 (2011) 011002.

[20] N. Sharpes, A. Abdelkefi, S. Priya, Comparative analysis of one-dimensional and two-dimensional cantilever piezoelectric energy harvesters. Energy Harvesting and Systems 1 (2014) 209-216.

[21] D.F. Berdy, P. Srisungsitthisunti, B. Jung, X. Xu, J.F. Rhoads, D. Peroulis, Low-frequency meandering piezoelectric vibration energy harvester. IEEE transactions on ultrasonics, ferroelectrics, and frequency control 59 (2012) 846-858.

[22] N. Sharpes, A. Abdelkefi, S. Priya, Two-dimensional concentrated-stress low-frequency piezoelectric vibration energy harvesters. Applied Physics Letters 107 (2015) 093901.

[23] C. Hindrichsen, R. Lou-Møller, K. Hansen, E.V. Thomsen, Advantages of PZT thick film for MEMS sensors. Sensors and Actuators A: Physical 163 (2010) 9-14.

[24] Q.R. Xu, Energy Harvesting Enabled Electric Current and Voltage Sensing Systems, University of California, Berkeley, 2014.

[25] K&J Magnetics, https://www.kjmagnetics.com/proddetail.asp?prod=B228

[26] H. Debéda, P. Clément, E. Llobet, C. Lucat, One-step firing for electroded PZT thick films applied to MEMS. Smart Materials and Structures 24 (2015) 025020.

[27] Fernandes E, Zarabi S, Debéda H, Lucat C, Nairn D, Wei L, Salehian A, Modelling and fabrication of a compliant centrally supported meandering piezoelectric energy harvester using screenprinting technology, Journal of Physics: Conference Series, 2016, pp. 012109.

[28] AK Steel, http://www.aksteel.com/pdf/markets_products/stainless/austenitic/AK%20301%20Stainless%20Steel%20PDB.pdf

[29] C. Castille, Etude de MEMS piézoélectriques libérés et microstructurés par sérigraphie.Application à la détection en milieu gazeux et en milieu liquide (2010).

[30] Harry Wad, https://commons.wikimedia.org/w/index.php?curid=2215242

[31] www.dek.com

[32] Inc The Modal Shop. 75 lbf dual purpose shaker, 2014.

[33] LMS. Lms scadas mobile, 2014.

[34] PCB Piezotronics. Model: 352a24 product specifications, 2014.

[35] Polytec Advanced Measurements by Light. Ofv-50x vibrometer sensor head and controller, 2014.

[36] D.J. Inman, Engineering vibration. (2014).

[37] D. Shen, J. Park, J. Ajitsaria, S. Choe, H.C. Wikle III, D. Kim, The design, fabrication and evaluation of a MEMS PZT cantilever with an integrated Si proof mass for vibration energy harvesting. Journal of Micromechanics and Microengineering 18 (2008) 055017.

[38] W. Chen, Y. Cao, J. Xie, Piezoelectric and electromagnetic hybrid energy harvester for powering wireless sensor nodes in smart grid. Journal of Mechanical Science and Technology 29 (2015) 4313-4318.

Appendix

A - Improving the geometry for low frequency MEMS Energy harvesting

The quad-folded cantilever design used by [7] utilizes four beams that are folded around in a spiral shape and attach to a mass at the end (Figure 50). The geometry contains four fixed constraints (one in each corner) and the tip mass acts like a guided end because of the symmetry. Stress analysis of the structure shows that each beam segment experiences both tension (red) and compression (blue), and a large areas exist where very little stress (grey) is experienced. The combination of both tension and compression in a single beam segment requires complicated electrode patterning for energy harvesting to ensure minimal voltage cancellation. Further, as the charge produced by the piezoelectric material is proportional to the stress induced in the beam it is highly undesirable for there to be large areas of the geometry that experience minimal stress. Moreoever, due to the spiral shape the structure experiences both torsion and bending and as mentioned earlier, torsional stresses are not readily harvestable.

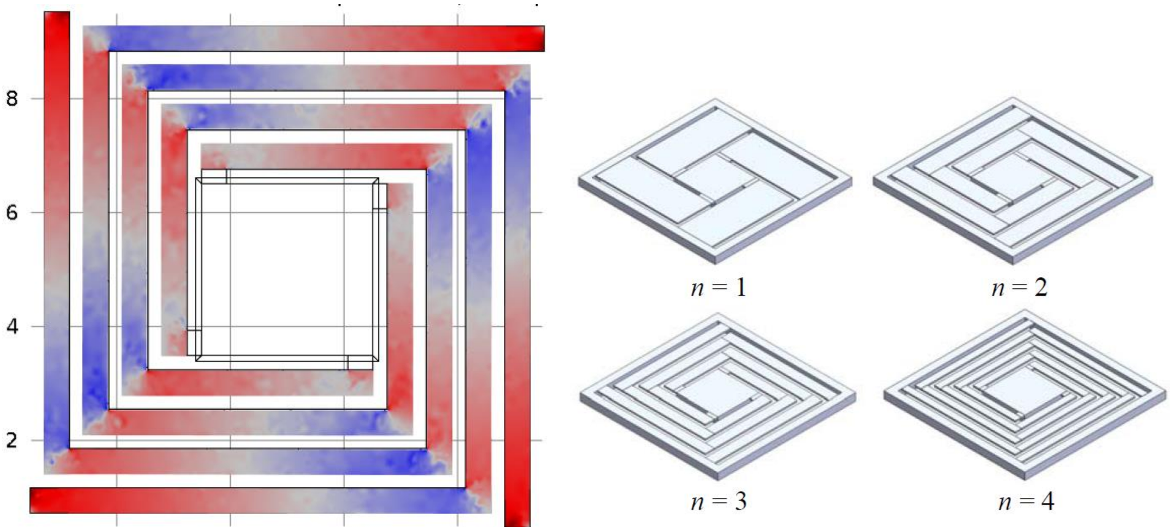

Figure 50: Quad-folded cantilever stress plot and assembly for n = 1, 2, 3, 4

The centrally supported meandering geometry (CSM) is a fixed-free design similar to a cantilever, shown in Figure 51. The center beam is clamped at one end and extends into zigzag pattern and wraps around to form a closed loop which supports a tip mass. Like a cantilever beam, this structure experiences the greatest amount of stress near its clamped end. The symmetry of this design reduces torsion in the center beam and results in greater bending that results in more efficient energy harvesting. Important to note is that each beam segment experiences either tension or compression and permits a single continuous electrode for each beam allowing for full utilization of the piezoelectric material. The structure also has very predictable strain nodes that are located at the ends of each beam. This is a major advantage with screen-printing fabrication as the known strain nodes can be avoided.

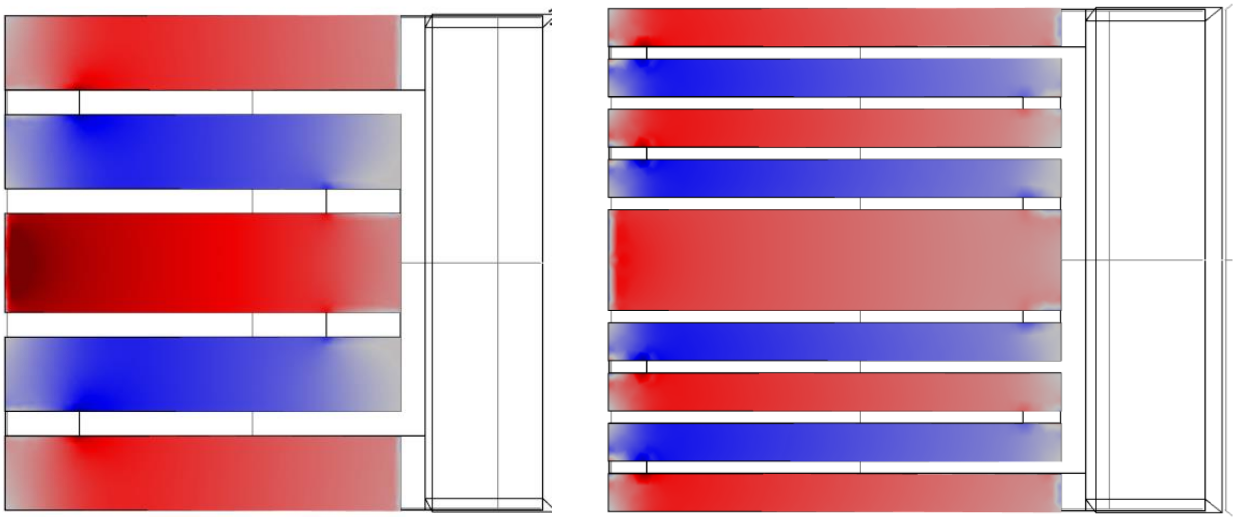

Figure 51: Centrally supported meandering geometry with 5 beams (left) and 9 beams (right)

The quad-folded geometry was compared with variations of the CSM geometry to determine which would be better for piezoelectromagnetic energy harvesting close to 60 Hz. Both designs used PZT-5A as the piezoelectric material and silicon for the substrate. The CMS designs offer a greater harvestable area, higher bending, and overall greater power output per area as shown in Table 9. For the reasons mentioned, the CSM was further optimized and chosen for this application.

Table 9: Comparison of quad-folded and centrally-supported meandering designs

	Quad-folded	**9 Beams**	**5 Beams**	**Optimized Design**
Eigenfrequency	56.526 Hz	56.394	56.609	56.76
Optimal Load	1E4 Ohm	5E4 Ohm	1E4 Ohm	1E4 Ohm
Freq @ opt load	56.53 Hz	56.58	57.82 Hz	56.79 Hz
Power @ opt load	3.1uW	11.2uW	11.8uW	22.4uW
Footprint	10x10=100mm^2	11.88x10=119mm^2	10x10.5=105mm^2	12.7x15=191mm^2
Power/Footprint	0.03 uW/mm^2	0.094 uW/mm^2	0.112 uW/mm^2	0.117 uW/mm^2
Force on magnet	2.5521E-4N	2.5521E-4N	2.5521E-4N	2.7553E-4N
Fixed Ends	4	1	1	1
PZT Thickness	1 um	181 um	62 um	70 um

Area of PZT	38.9375mm^2	72 mm^2	64 mm^2	84.125 mm^2
Area of electrodes	20.68 mm^2	72 mm^2	64 mm^2	84.125 mm^2
AE/AP	53%	1	1	1
Volume of PZT	38.9375mm^3	13,032 mm^3	3,968 mm^3	5,889 mm^3
RMS Current @Rl	0.007428mA	.015363 mA	.033455 mA	0.047276 mA
RMS Voltage @Rl	0.07428 V	0.76813 V	0.33455 V	0.47276 V